Intraflagellar transport complex B proteins regulate the Hippo effector Yap1 during cardiogenesis

Marina Peralta[1,2,3,4], Katerina Jerabkova[1,2,3,4]*, Tommaso Lucchesi[5,6,7]*, Laia Ortiz Lopez[1,2,3,4], Benjamin Vitre[8], Dong Han[5,6], Laurent Guillemot[5,6], Chaitanya Dingare[9], Izabela Sumara[1,2,3,4], Nadia Mercader[10,11], Virginie Lecaudey[9], Benedicte Delaval[8], Sigolène M. Meilhac[5,6] and Julien Vermot[1,2,3,4]

[1]Institut de Génétique et de Biologie Moléculaire et Cellulaire, Illkirch, France

[2]Centre National de la Recherche Scientifique, UMR7104, Illkirch, France

[3]Institut National de la Santé et de la Recherche Médicale, U964, Illkirch, France

[4]Université de Strasbourg, Illkirch, France

[5]*Imagine* - Institut Pasteur, Laboratory of Heart Morphogenesis, Paris, France

[6]INSERM UMR1163, Université Paris Descartes, Paris, France

[7]Sorbonne Université, Collège Doctoral, F-75005, Paris, France

[8]Centre de Recherche en Biologie cellulaire de Montpellier, (CRBM), CNRS, Univ. Montpellier, Montpellier, France

[9]Institute for Cell Biology and Neurosciences, Goethe University of Frankfurt, Germany

[10]Institute of Anatomy, University of Bern, Switzerland

[11]Centro Nacional de Investigaciones Cardiovasculares CNIC, Madrid, Spain

*equal second authors listed in alphabetical order.

Abstract

Cilia and the intraflagellar transport (IFT) proteins involved in ciliogenesis are associated with congenital heart diseases (CHD). However, the molecular links between cilia, IFT proteins and cardiogenesis are yet to be established. Using a combination of biochemistry, genetics, and live imaging methods, we show that IFT complex B proteins (Ift88, Ift54 and Ift20) modulate the Hippo pathway effector YAP1 in zebrafish and mouse. We demonstrate that this interaction is key to restrict the formation of the proepicardium and the myocardium. *In cellulo* experiments suggest that IFT88 and IFT20 interact with YAP1 in the cytoplasm and functionally modulates its activity, identifying a molecular link between cilia related proteins and the Hippo pathway. Taken together, our results highlight a novel role for IFT complex B proteins during cardiogenesis and shed light on an unexpected mechanism of action for ciliary proteins in YAP1 regulation. These findings provide mechanistic insights into a non-canonical role for cilia related proteins during cardiogenesis.

Introduction

Primary cilia are immotile microtubule-based organelles, well known for being both chemical and/or mechanical sensors (1). Disruption of cilia function causes multiple human syndromes known as ciliopathies (2). Cilia are required for cardiac development and mutations in cilia-related proteins have been linked to congenital heart diseases (CHDs) (3–6). Nevertheless, the specific role of cilia and cilia-related proteins during cardiogenesis is still unclear.

51 Intraflagellar transport (IFT) proteins are required for the transport of cilia components along
52 the axoneme and are thus essential for cilia formation and function (7). The role of IFT proteins
53 during ciliogenesis is highly conserved across organisms (8). The IFT machinery is composed
54 of two biochemically distinct subcomplexes, IFT-A and IFT-B (8). The IFT complex B member
55 IFT20, which localizes inside the cilium and at the Golgi complex in mammalian cells,
56 participates in the sorting and/or transport of membrane proteins for the cilia (9). Within the
57 IFT complex B, IFT20 interacts with IFT54/Elipsa (10,11), and IFT88 which is essential for
58 flagellar assembly in *Chlamydomonas* and ciliogenesis in vertebrates (12). Mutations in IFT
59 proteins lead to ciliary defects and to several ciliopathies (2). Importantly, some IFT proteins
60 have been identified in CHDs(4). IFT proteins also display non-canonical, cilia-independent
61 functions (13,14). IFT88, for example, is needed for spindle orientation or cleavage furrow
62 ingression in dividing cells (15,16) and regulates G1-S phase transition in non-ciliated cells
63 (17). IFT20, together with IFT88 and IFT54, plays a role in the establishment of the immune
64 synapse in T-lymphocytes lacking cilia (18,19). These observations suggest that IFT proteins
65 could play a key role in embryonic cardiogenesis through both cilia-dependent and –
66 independent functions.
67 The Hippo signaling mediators, YAP1/WWTR1 (TAZ), constitute a key signaling pathway for
68 the regulation of cardiac development (20–23) and cardiac regeneration (24,25) in vertebrates.
69 For example, YAP1/WWTR1 (TAZ) are required for epicardium and coronary vasculature
70 development (26) in mice. Changes in cell shape, substrate stiffness and tension forces activate
71 a phosphorylation-independent YAP1/WWTR1 (TAZ) modulation (27) which is mediated by
72 the Motin family (AMOT, AMOTL1, and AMOTL2) (28,29). Motin proteins bind to
73 YAP/WWTR1 (TAZ) sequestering them in the cytoplasm in several cellular contexts (30–34).
74 While it is known that ciliary proteins from the Nephrocystin family modulate the
75 transcriptional activity of YAP1/WWTR1 (TAZ) (35–37) and that the Hippo kinases MST1/2-

76 SAV1 pathway promotes ciliogenesis (38), the connection between the Hippo pathway and cilia
77 function remains unclear.
78 Cardiogenesis involves an interplay between multiple tissue layers. The epicardium is the
79 outermost layer covering the heart. This cardiac cell layer plays an essential role in myocardial
80 maturation and coronary vessel formation during development (39–41) and has a crucial role
81 during regeneration (42–44). Epicardial cells derive from the proepicardium (PE), an extra-
82 cardiac transient cluster of heterogeneous cells (45). In mice, the PE is a single cell cluster
83 located close to the venous pole of the heart (45), while in zebrafish is composed by two cell
84 clusters, avcPE (the main source of cells) and vpPE (46). Proepicardial cells give rise to the
85 epicardium, part of the coronary vasculature and intracardiac fibroblasts (45,47–49). The
86 secreted signaling molecules of the bone morphogenetic protein (BMP) family are
87 indispensable for PE formation (50–52). However, the regulation of PE development remains
88 poorly understood.
89 Despite the increasing evidence for the role of IFT proteins in cell signaling, it has been difficult
90 to pinpoint the exact function of cilia-related proteins outside the cilium. Without this key
91 information, the question of whether cilia-related proteins can affect the developmental
92 program independently of their cilia function remains unresolved. Here, we provide a
93 combination of *in vivo* and *in vitro* analyses of IFT protein function showing that IFT complex
94 B proteins can modulate the Hippo pathway effector Yap1. In particular, we show that IFT88
95 is required to restrict proepicardial and myocardial development through cytoplasmic activity.
96
97 ***Results***
98 *IFT complex B proteins regulate proepicardial development in zebrafish and mouse.*
99 Considering the importance of cilia during cardiogenesis, we assessed the role of several IFT
100 complex B proteins during embryonic cardiogenesis *in vivo* focusing on the PE. In order to

101 benefit from live imaging and genetics, we used zebrafish as a model organism. We performed
102 live imaging focusing on the main PE cell source located near the atrioventricular canal (avcPE)
103 in *ift88* (53) and *elipsa/ift54* (10) mutants (**Fig. 1 A-D**) (**Supp. 1 B, C**). Between 50 hpf and 57
104 hpf, we found that *ift88* mutants display multiple avcPE clusters (either 2 or 3), when controls
105 have only one (**Movie 1**). Using a *wilms tumor 1 a* (*wt1a)* enhancer trap line that marks
106 proepicardial and epicardial cells *(Et(-26.5Hsa.WT1-gata2:EGFP)*^{cn1} hereafter *epi:GFP)* (46)
107 we quantified avcPE and epicardial cell number and found that *ift88*$^{-/-}$ have increased avcPE
108 cell numbers compared to their controls at 50 hpf. We additionally found that the size change
109 is associated with an increased number of epicardial cells number in *ift88*$^{-/-}$ embryos (**Supp. 2**
110 **A)**. Similarly, we found that *elipsa*$^{-/-}$ also showed bigger avcPE compared to controls (**Fig. 1 D**)
111 (**Supp. 1 A'')**. Taken together, these data indicate that *ift88* and *elipsa*/*ift54* are required to
112 restrict PE size.
113 To determine whether primary cilia are required for PE formation, we took advantage of the
114 *iguana/dzip* (54) mutant, a well-established cilia mutant lacking primary cilia (55). We
115 confirmed the absence of primary cilia in the pericardial cavity of the *iguana*$^{-/-}$ using the cilia
116 reporter *actb2:Mmu.Arl13b-GFP* (56) (**Supp. 2 C-E**) (**Movie 2**). Zebrafish *ift* genes are
117 expressed maternally (57) (**Supp. 2 E**) and complete removal of both zygotic and maternal
118 expression of *ift88* leads to the ablation of primary cilia resembling the *iguana* mutant
119 phenotype (58). Live imaging revealed that a significant fraction of *iguana* mutants lacked an
120 avcPE between 50 hpf and 57 hpf (**Fig. 1 B**) (**Movie 3**). At 55 hpf, *iguana*$^{-/-}$ displayed decreased
121 avcPE cell numbers (**Fig. 1 D**) (**Supp. 1 A and 2 A')**. Since the *iguana* mutants presented a
122 phenotype opposite to that of the *ift88* mutants, we analyzed the *ift88*$^{-/-}$*; iguana*$^{-/-}$*; epi:GFP*
123 double mutant to elucidate whether the differences could be due to a new cilia-independent
124 function. The *ift88*$^{-/-}$*; iguana*$^{-/-}$*;* double mutant shows multiple avcPE cluster formation and an

125 increased avcPE cell number, reminiscent of *ift88* loss of function (**Fig. 1 E, F**) (**Supp. 1 D)**.
126 We conclude that Ift88 modulates the PE cell number independently of its cilia function.
127 We next assessed whether the role of IFT complex B proteins during PE formation was
128 conserved in mammals. We analyzed the PE in *Ift20* and *Ift88* knock-out (KO) mice at mouse
129 embryonic day (E) 9.5 (**Fig. 1 G, H**) (**Supp. 3 A, B)**. First, we performed immunofluorescence
130 using an anti-Arl13b antibody to quantify the percentage of ciliated PE cells in *Ift20*, *Ift88 KO*
131 and *wild type* mice (**Supp. 3 C-C''**). We found that, while over 60% of the *wild type* PE cells
132 were ciliated, in *Ift88 KO* mice only 3% of PE cells were ciliated and *Ift20 KO* embryos lack
133 cilia (**Supp. 3 C''**). We compared the PE volume of *Ift20 KO* mice to their controls , using an
134 anti-Wt1 antibody (a well-established PE marker (59)). Mutant embryos showed increased PE
135 volume compare to controls (**Movie 5, 6**). Likewise, the PE volume in *Ift88 KO* was also
136 increased compared to controls (**Fig. 1 H**).Together, these results suggest that IFT protein
137 function is conserved during PE formation in mouse and zebrafish and that, in zebrafish, IFT88
138 contributes to this process independently of its ciliary function.
139 To test whether IFT complex B affected other cardiac tissues, we focused in the myocardium.
140 Cell quantification showed increased myocardial cell number in *ift88*$^{-/-}$ compared to their
141 controls at 50 hpf (**Fig. 2 A, A'**) and 55 hpf (**Supp. 4 A**). Interestingly, the increment was mostly
142 affecting the atrium. Similar data were obtained with the *elipsa* mutants at 55hpf (**Fig. 2 B**).
143 These results led us to conclude that the absence of IFT complex B proteins also affects the
144 myocardial cells.
145
146

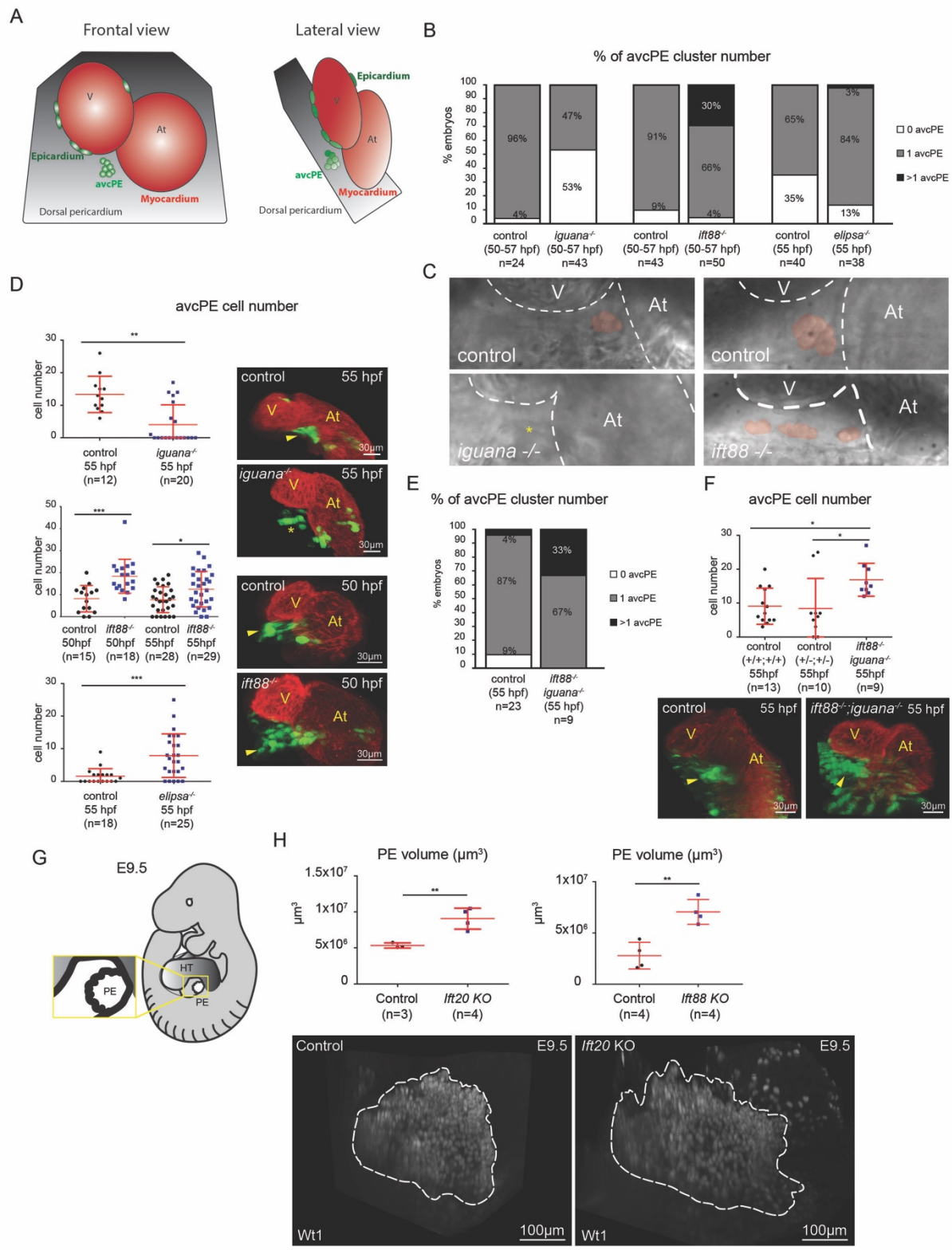

Figure 1. IFT complex B proteins regulate proepicardial development in zebrafish and mice. ***(A)*** *Schematic representation of the zebrafish heart at 55 hpf in frontal and lateral views. The dorsal pericardium is shown in grey, the myocardium in red, the avcPE in light green and the*

151 *epicardial cells in dark green. V, ventricle; At, atrium.**(B)** Percentage of avcPE cluster number*
152 *in iguana (n=43), ift88 (n=50) and elipsa/ift54 (n=38) mutants and their controls (n=24; n=43;*
153 *n=40 respectively), between 50 and 57 hpf.* ***(C)*** *High-speed avcPE imaging (digital red mask*
154 *to improve visualization) of iguana and ift88 mutants and their control.* ***(D)*** *Graphs show avcPE*
155 *cell number quantified on iguana (n=20), ift88 (n=18 and 29) and elipsa (n=25) mutants in*
156 *epi:GFP background and their controls (n=12; n=15; n=28 n=18 respectively). (t-test iguana*
157 *p-value 0.001; ift88 p-value 0.0002 and p-value 0.015 respectively; elipsa p-value 0.0005). 3D*
158 *projections of whole mount immunofluorescence of hearts using an anti-myosin heavy chain*
159 *antibody (red) and GFP (green) expression. Ventral views, anterior is to the top. Arrowheads*
160 *mark avcPE and asterisk shows lack of avcPE.* ***(E)*** *Percentage of avcPE cluster number on*
161 *iguana$^{-/-}$, ift88$^{-/-}$, epi:GFP (n=9) and controls (n=23) at 55 hpf.* ***(F)*** *Graph shows avcPE cell*
162 *number quantified in wild type (n=13) and double heterozygous controls (n=10) (ift88$^{+/+}$;*
163 *iguana$^{+/+}$; epi:GFP and ift88$^{+/-}$; iguana$^{+/-}$; epi:GFP) and double ift88; iguana mutants (n=9)*
164 *(ift88$^{-/-}$; iguana$^{-/-}$; epi:GFP) (Kruskal-Wallis p-value 0.014) . 3D projections of whole mount*
165 *immunofluorescence of hearts using myosin heavy chain antibody (red) and GFP (green)*
166 *expression. Ventral views, anterior is to the top. Arrowheads mark avcPE. V, ventricle; At,*
167 *atrium.* ***(G)*** *Schematic representation of an E9.5 mouse embryo. Heart tube (HT) in dark grey*
168 *and PE in white. Section of the PE represented inside the yellow box.* ***(H)*** *Left side graph shows*
169 *quantification of PE volume (µm3) in Ift20 KO (n=4) and control mice (n=3) (control*
170 *5.35x10^{6}µm^{3}±3.63x10^{5}; Ift20 KO 9.06x10^{6}µm^{3}±1.46x10^{6}) (t-test p-value 0.008) and that of*
171 *Ift88 KO (n=4) and control embryo (n=4) on the right (control 2.78x10^{6}µm^{3}±1. 3x10^{6}; Ift88*
172 *KO 7.05x10^{6}µm^{3}±1.2x10^{6}) (t-test p-value 0.003). In the lower panel, 3D projections of*
173 *immunofluorescence whole-mount performed on control and Ift20 KO embryos. PE marked*
174 *using anti-Wt1 antibody. White dotted shapes enclose the PE area. In all graphs, red bars*
175 *indicate mean ± standard deviation.*

176

177 *BMP signaling is increased in ift88, elipsa/ift54 and Ift20 mutants during PE development.*

178 As it is known in zebrafish that overexpressing BMP increases PE size (50), we investigated
179 whether *ift88* loss influences BMP signaling. We first assessed *bmp4* expression by *in situ*
180 hybridization in *ift88* and *elipsa* mutants. We found that *ift88* mutant embryos display ectopic
181 expression of *bmp4* in the dorsal pericardium (DP) at 48 hpf (**Supp. 4 B**). To validate that the
182 upregulation is functional *in vivo*, we quantified cellular BMP activity by using p-smad 1/5 as
183 a readout and confirmed that the absence of Ift88 leads to increased BMP signaling activity
184 (**Fig. 2 D, D'**). Additionally, more myocardial cells were positive for p-smad 1/5 in *ift88*$^{-/-}$ than
185 in controls, especially in the venous pole (**Fig. 2 D, D'**) (**Supp. 4 C)**. By 55 hpf, *bmp4*
186 expression at the atrioventricular canal myocardium is reduced and the expression at the venous
187 pole is almost undetectable in controls. By contrast, *ift88* mutants presented strong *bmp4*
188 expression in both domains (**Supp. 4 B**). Myocardial p-smad 1/5 was also increased in *ift88*$^{-/-}$
189 compared to controls, but not in the DP (**Supp. 4 C, D)**. We reached similar conclusions when
190 analyzing the *elipsa* mutants at 55 hpf (**Fig. 2 E**) (**Supp. 4 B-C**). To confirm that the regulation
191 of BMP signaling by IFT is conserved in vertebrates, we next analyzed p-smad 1/5/9 in *Ift20*
192 and *Ift88 KO* and control mice at E9.5 and found that only the *Ift20* mutants displayed a higher
193 percentage of p-smad-positive cells compared to controls (**Fig. 2 G, G'**). (**Supp. 3 D**). Together,
194 these results suggest that Ift88 and Ift54 modulate BMP signaling activity in the myocardium
195 and the pericardium of the zebrafish, and that IFT20 plays a similar role in the mouse PE.

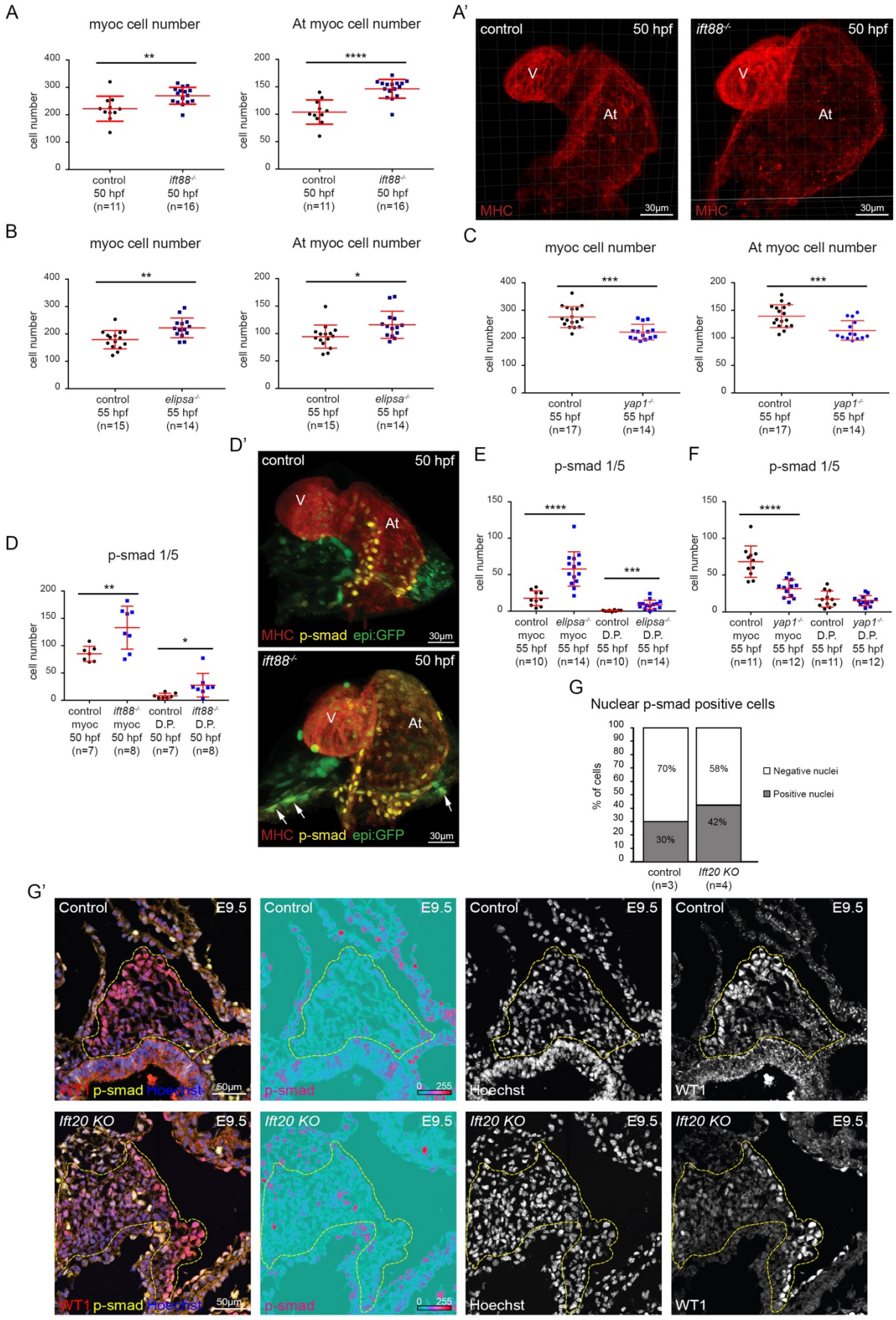

196

197 ***Figure 2. BMP signaling is increased in ift88, elipsa/ift54 and Ift20 mutants.***

198 ***(A)*** *Graphs show total myocardial and atrial-myocardial cell number quantified in ift88 (n=16)*
199 *mutants and controls (n=11) at 50 hpf. (t-test total myocardium p-value 0.0034; atrial*
200 *myocardium p-value <0.0001).* ***(A')*** *3D projections of whole mount immunofluorescence of*
201 *hearts using myosin heavy chain antibody (MHC) (red). Ventral views, anterior is to the top.*
202 ***(B)*** *Graphs show total myocardial and atrial-myocardial cell number quantified in elipsa*
203 *(n=14) mutants and controls (n=15) at 55 hpf. (t-test total myocardium p-value 0.0026; atrial*
204 *myocardium p-value 0.017).* ***(C)*** *Graphs show total myocardial and atrial-myocardial cell*
205 *number quantified in yap1 (n=14) mutants and controls (n=17) at 55 hpf. (t-test total*
206 *myocardium p-value 0.0001; atrial myocardium p-value 0.0009).* ***(D)*** *Graph shows number of*
207 *p-smad1/5 positive cells in the myocardium and dorsal pericardium (DP) quantified in ift88*
208 *mutants (n=8) and controls (n=7) at 50 hpf. Myocardium (t-test p-value 0.009) and DP (t-test*
209 *p-value 0.036).* ***(D')*** *3D projections of whole mount immunofluorescence of hearts using myosin*
210 *heavy chain antibody (MHC) (red), epi:GFP (green) and p-smad1/5 (yellow) antibody. Arrows*
211 *mark dorsal pericardial cells positive for epi:GFP and p-smad1/5. Ventral views, anterior is to*
212 *the top.* ***(E)*** *Graph shows number of p-smad1/5 positive cells in the myocardium and dorsal*
213 *pericardium (DP) quantified in elipsa mutants (n=14) and controls (n=10) at 55 hpf.*
214 *Myocardium (t-test p-value < 0.0001) and DP (t-test p-value 0.0004).* ***(F)*** *Graph shows number*
215 *of p-smad1/5 positive cells in the myocardium and dorsal pericardium (DP) quantified in yap1*
216 *mutants (n=12) and controls (n=11) at 55 hpf. Myocardium (t-test p-value < 0.0001) and DP*
217 *(t-test p-value 0.599).* ***(G)*** *Graph shows that the percentage of p-smad 1/5/9 positive PE cells*
218 *is higher in Ift20 KO (n=4 embryos: 1862 nuclei analyzed) compared to control (n=3 embryos:*
219 *1414 nuclei analyzed) mice (Chi-square test* of homogeneity *=51.593, p-value 6.829e-13 on 1*
220 *degree of freedom).* ***(G')*** *Control and Ift20 KO immunofluorescence confocal cryosections*
221 *labelled with WT1 (red), p-smad 1/5/9 (yellow) and Hoechst (blue) at E9.5. Yellow dotted lines*
222 *enclose the PE area. Individual channels are displayed for p-smad 1/5/9 (signal is shown as*

223 *ice LUT to facilitate the visualization of signal intensity, where green is the minimum and red*
224 *is the maximum), Hoechst (white) and WT1 (white). In all graphs, red bars indicate mean ±*
225 *standard deviation. V, ventricle; At, atrium. p-smad, p-smad1/5 in panel D'and p-smad1/5/9 in*
226 *panel G'.*
227
228 *Yap1-Tead activity is increased in ift88, elipsa/ift54 and Ift20 mutants during PE development.*
229 YAP1/WWTR1, which are important regulators of tissue size (60), are essential for epicardium
230 and coronary vasculature development (26). In addition, Yap1 participates in the regulation of
231 Bmp signaling during secondary heart field development (21). This led us to assess if
232 Yap1/Wwtr1-Tead is active during PE formation. We first analyzed Yap1/Wwtr1-Tead activity
233 in PE cells using the *4xGTIIC:d2GFP* reporter line (61). We found that the reporter was active
234 in the PE cluster, myocardium, pericardium and epicardial cells at 55 hpf (**Supp. 5 A**). Time-
235 lapse analysis allowed us to evaluate the dynamics of Yap1/Wwtr1-Tead activity during PE
236 development between 51 and 60 hpf (**Movie 4**) (**Supp. 5 B**). GFP quantification in PE and
237 pericardial cells showed higher Yap1/Wwtr1-Tead activity (GFP average intensity) in the PE
238 cells than in the pericardial cells (75% of the embryos) (**Supp. 5 B**) (**Supp. Table 1**). Thus,
239 Yap1/Wwtr1-Tead is active in PE cells during PE development.
240 We next tested whether the increased avcPE cell number was due to abnormal Yap1 activity,
241 we performed immunofluorescence to quantify the number of nuclear Yap1-positive cells in
242 *ift88* and *elipsa* mutants (**Fig. 3A, A'**) (**Supp. 6 A-B'**). At 55 hpf, *ift88*$^{-/-}$ showed more nuclear
243 Yap1-positive cardiomyocytes than controls (**Fig. 3 A**), especially in the atrium (**Supp. 6 A**).
244 Similar data were obtained with the *elipsa* mutants (**Fig. 3 A**) (**Supp. 6 A**). To further validate
245 the link between increased PE size and Yap1-Tead activity, we treated the *ift88* mutants with
246 the drug Verteporfin, which binds to YAP and changes its conformation, blocking its interaction
247 with TEAD (62). We first performed time-lapse imaging on Verteporfin treated

248 *4xGTIIC:d2GFP* embryos at 55 hpf to assess Verteporfin specificity. We measured the
249 Yap/Wwtr1-Tead activity (GFP average intensity) in the same PE and pericardial cells at
250 several timepoints: before adding Verteporfin (t0), after 2 hours treatment with Verteporfin
251 (5µM), and 45 min after washing out (**Supp. 5 C**). We found that Yap/Wwtr1-Tead activity is
252 significantly decreased with Verteporfin, confirming the specificity of the drug on the embryo.
253 We next treated *ift88*$^{-/-}$ and control (*ift88*$^{+/+}$ and $^{+/-}$) embryos with Verteporfin (5µM) from 50
254 hpf to 55 hpf (**Fig. 3 B**). Control embryos treated with Verteporfin showed smaller avcPE
255 compared to untreated controls. Verteporfin-treated *ift88*$^{-/-}$ embryos presented fewer avcPE cell
256 numbers than non-treated *ift88*$^{-/-}$ embryos. Interestingly, non-treated controls and treated *ift88*
257 mutants did not show significant differences in avcPE cell number. Thus, the increase in avcPE
258 cell number induced in the absence of Ift88 was rescued by Verteporfin treatment. These results
259 suggest that Ift88 requires Yap1 activity to modulate the PE size restriction.
260 Additionally, to explore a possible role of Yap1 in the regulation of BMP signaling by IFT, we
261 treated *ift88*$^{-/-}$ and control (*ift88*$^{+/+}$ and $^{+/-}$) embryos with Verteporfin (20µM) from 31 hpf to 55
262 hpf (**Fig. 3 C**). We quantified cellular BMP activity by using p-smad 1/5 as a readout. Control
263 embryos treated with Verteporfin showed decreased p-smad 1/5-positive myocardial cell
264 number compared to untreated controls. Verteporfin-treated *ift88*$^{-/-}$ embryos presented fewer p-
265 smad 1/5-positive myocardial cells than non-treated *ift88*$^{-/-}$ embryos. Remarkably, non-treated
266 controls and treated *ift88* mutants did not show significant differences in p-smad 1/5-positive
267 myocardial cells. Thus, the increase in BMP activity induced in the absence of Ift88 was rescued
268 by Verteporfin treatment. Likewise, *in situ* hybridization performed in *elipsa*$^{-/-}$ and control
269 (*elipsa*$^{+/+}$ and $^{+/-}$) embryos treated with Verteporfin (20µM) from 31 hpf to 55 hpf displayed
270 decreased *bmp4* expression (**Supp. 6 C**). Furthermore, treatment with the drug XAV939
271 (10µM), a tankyrase inhibitor that suppressed YAP-TEAD activity (63) also lead to a reduction
272 of *bmp4* expression (**Supp. 6 C**). These results suggest that Ift88 and Ift54 require Yap1 activity

273 to modulate BMP signaling activity in the myocardium of the zebrafish. To confirm the
274 involvement of an increased Yap1 activity in the *ift88* mutant phenotype, we analyzed the
275 avcPE in *angiomotin like 2a* (*amotl2a*) mutants (**Fig. 3 D, E**). In zebrafish, Amotl2a physically
276 interacts with Yap1 leading to its cytoplasmic retention in a way that *amotl2a* mutants show
277 upregulated Yap1 activity (nuclear Yap1) (33,34). Accordingly, *amotl2a*$^{-/-}$ presented multiple
278 avcPE formation. In addition, *bmp4* expression was increased in *amotl2a*$^{-/-}$ when compared to
279 *amotl2a*$^{+/+}$ embryos at 55 hpf. These data are consistent with the *ift88* mutant phenotype and
280 suggest that Ift88 modulates Yap1 activity to restrict PE size. To further validate the link
281 between increased Yap1 and BMP signaling activity, we treated the *amotl2a* mutants with the
282 drug Verteporfin (20µM) from 31 hpf to 55 hpf (**Fig. 3 F, F'**). *amotl2a*$^{-/-}$ embryos treated with
283 Verteporfin showed decreased p-smad 1/5-positive myocardial cell number and avcPE cells
284 compared to untreated *amotl2a*$^{-/-}$ embryos. Likewise, *bmp4* expression at the atrioventricular
285 canal myocardium and at the venous pole were reduced in *amotl2a*$^{-/-}$ embryos treated with
286 XAV939 (10µM) from 31 hpf to 55 hpf, when compared to untreated *amotl2a*$^{-/-}$ embryos (**Fig.
287 3 G**). Thus, Verteporfin and XAV939 treatments rescued the increase in BMP signaling induced
288 in the absence of Amotl2a suggesting it acts through Yap1 activity. To further confirm the link
289 between Yap1 activity and PE formation, we next analyzed the *yap1* mutants (33). At 55 hpf,
290 *yap1*$^{-/-}$ showed decreased myocardial cell number compared to their controls (**Fig. 2 C**). Besides,
291 fewer myocardial cells were positive for p-smad 1/5 in *yap1* mutants (**Fig. 2 F**). Surprisingly,
292 avcPE cell number was similar between *yap1*$^{-/-}$ and their controls (**Supp. 2 B, B'**). Altogether,
293 these results suggest that Ift88 and Ift54 modulate BMP signaling activity by tuning Yap1-Tead
294 activity in the myocardium of the zebrafish. To assess if the upregulation of Yap1 activity
295 observed in IFT zebrafish mutants was conserved in vertebrates, we analyzed YAP1
296 localization in the PE of *Ift20 KO* and control mice (**Fig. 3 H-H''**). We quantified the proportion
297 of nuclear YAP1-positive cells (i.e. cells with higher signal intensity inside the nucleus than in

298 the cytoplasm) (**Fig. 3 H''**). The percentage of nuclear YAP1-positive PE cells was higher in
299 *Ift20 KO* than in control mice (**Fig. 3 H**). In mouse cardiomyocytes, YAP1 and AMOTL1
300 translocate to the nucleus together to modulate cell response (23). To assess AMOTL1
301 localization in PE cells, we performed AMOTL1 immunofluorescence. Consistent with the
302 results obtained with an anti-YAP1 antibody, the percentage of nuclear AMOTL1-positive cells
303 (i.e. cells with higher signal intensity inside the nucleus than in the cytoplasm) was increased
304 in the *Ift20 KO* when compared to control mice (**Supp. 6 D**). We also found that the mutants
305 showed an increase in the percentage of YAP1–AMOTL1 double positive cells (**Fig. 3 H**).
306 Together, these data show that the increased PE size in *Ift20 KO* mice is associated with
307 increased YAP1 activity.
308

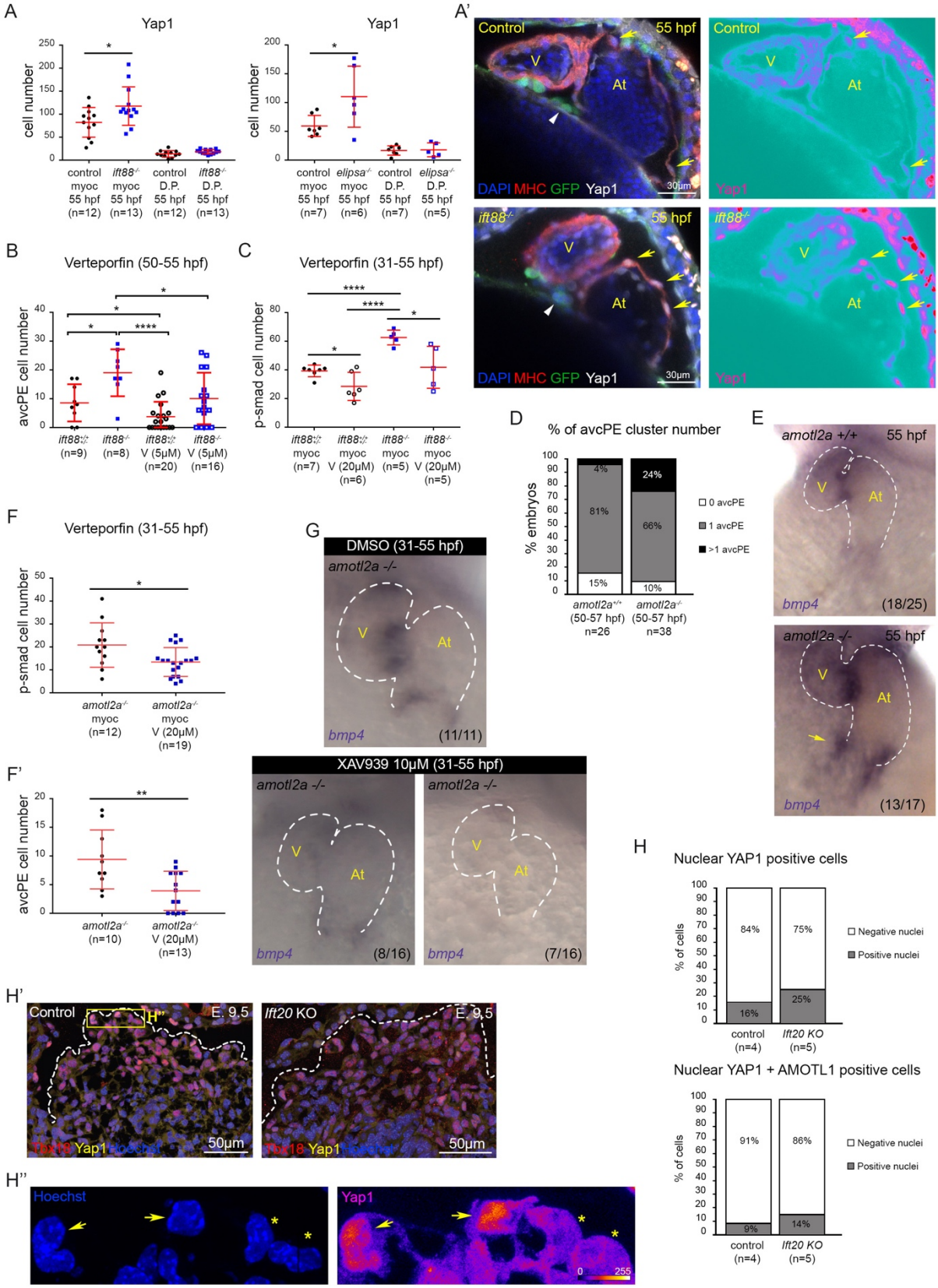

309

310 ***Figure 3. Yap1-Tead activity is increased in ift88, elipsa/ift54 and Ift20 mutants during***

311 ***proepicardium development.***

312 ***(A)*** *Graphs show number of Yap1-positive cells in the myocardium and dorsal pericardium*
313 *(DP) quantified in ift88 (n=13), elipsa (n=6) and their controls (n=12 and n=7 respectively).*
314 *ift88 mutants show increased Yap1-positive myocardial cell numbers (t-test p value 0.03) and*
315 *a tendency towards higher Yap1 positive DP cell numbers (t-test p value 0.07). elipsa mutants*
316 *show higher Yap1-positive myocardial cell numbers (t-test p value 0.036).* ***(A')*** *Control and*
317 *ift88$^{-/-}$, epi:GFP immunofluorescence confocal sections labelled with anti-myosin heavy chain*
318 *antibody (MHC) (red), GFP (green),-Yap1 (white) and DAPI (blue) at 55 hpf. Ventral view,*
319 *anterior is to the top. Individual channel is displayed for Yap1 (signal is shown as ice LUT to*
320 *facilitate the visualization of signal intensity, where green is the minimum and red is the*
321 *maximum). Yellow arrows mark nuclear Yap1-positive atrial myocardial cells. White*
322 *arrowheads mark the avcPE.* ***(B)*** *Graph shows avcPE cell number quantified in control (n=9),*
323 *ift88$^{-/-}$, epi:GFP (n=8) and Verteporfin (5µM)-treated ift88$^{-/-}$, epi:GFP (n=16) and control*
324 *(n=20) embryos (55hpf). Control embryos treated with Verteporfin showed smaller avcPE*
325 *compared to untreated controls (t-test p-value 0.04). Verteporfin-treated ift88$^{-/-}$; epi:GFP*
326 *embryos presented lower avcPE cell numbers than non-treated ift88$^{-/-}$; epi:GFP embryos (t-test*
327 *p-value 0.027). ift88$^{-/-}$; epi:GFP embryos showed bigger avcPE compared to untreated (t-test*
328 *p-value 0.01) and treated controls (t-test p-value 0.0001).* ***(C)*** *Graph shows number of p-smad*
329 *1/5-positive cells in the myocardium quantified in control (n=7), ift88$^{-/-}$, epi:GFP (n=5) and*
330 *Verteporfin (20µM)-treated ift88$^{-/-}$, epi:GFP (n=5) and control (n=6) embryos from 31 hpf to*
331 *55 hpf. Control embryos treated with Verteporfin showed decreased p-smad 1/5-positive cell*
332 *numbers compared to untreated controls (t-test p-value 0.0219). Verteporfin-treated ift88$^{-/-}$;*
333 *epi:GFP embryos presented less p-smad 1/5-positive cells than non-treated ift88$^{-/-}$; epi:GFP*
334 *embryos (t-test p-value 0.0173). ift88$^{-/-}$; epi:GFP embryos showed more p-smad 1/5-positive*
335 *cells compared to untreated (t-test p-value <0.0001) and treated controls (t-test p-value*
336 *<0.0001).* ***(D)*** *Percentage of avcPE cluster number in amotl2a$^{+/+}$ (n=26) and amotl2a$^{-/-}$ (n=38)*

337 *embryos between 50 and 57 hpf.* ***(E)*** *Whole mount bmp4 in situ hybridization in amotl2a*$^{+/+}$
338 *(n=18/25) and amotl2a*$^{-/-}$ *(n=13/17) embryos (55hpf). Yellow arrow shows bmp4*
339 *overexpression. Ventral views, anterior is to the top.* ***(F)*** *Graph shows number of p-smad 1/5-*
340 *positive cells in the myocardium quantified in Verteporfin (20µM)-treated amotl2a*$^{-/-}$ *(n=19)*
341 *embryos from 31 to 55 hpf and untreated amotl2a*$^{-/-}$ *(n=12) embryos. Treated embryos showed*
342 *decreased p-smad 1/5-positive cell numbers compared to untreated ones (t-test p-value 0.0148).*
343 ***(F')*** *Graph shows avcPE cell number quantified in Verteporfin (20µM)-treated amotl2a*$^{-/-}$
344 *(n=13) embryos from 31 to 55 hpf and untreated amotl2a*$^{-/-}$ *(n=10) embryos. Treated embryos*
345 *showed decreased avcPE cell numbers compared to untreated ones (t-test p-value 0.0059).* ***(G)***
346 *Whole mount bmp4 in situ hybridization in XAV939 (10µM)-treated amotl2a*$^{-/-}$ *(n=16) from 31*
347 *to 55 hpf and untreated embryos (n=11). Treated embryos showed either decreased (n=8/16)*
348 *or absent (n=7/16) bmp4 expression at the atrioventricular canal myocardium and the venous*
349 *pole. Ventral views, anterior is to the top.* ***(H)*** *Graphs show percentages of YAP1-positive PE*
350 *cells and double YAP1-AMOTL1-positive PE cells in Ift20 KO (n=5 embryos: 1196 nuclei*
351 *analyzed) and control (n=4 embryos: 929 nuclei analyzed) mice at E9.5. The percentage of*
352 *nuclear YAP1-positive PE cells (Chi-square test* of homogeneity *=25.354, p-value 4,77E-07 on*
353 *1 degree of freedom) and nuclear YAP1-AMOTL1-positive cells (Chi-square test* of
354 homogeneity *=12,025, p-value 5,25E-04 on 1 degree of freedom) were higher in Ift20 KO than*
355 *in control mice.* ***(H')*** *Control and Ift20 KO immunofluorescence confocal cryosections labelled*
356 *with TBX18 (red), YAP1 (yellow) and Hoechst (blue) at E9.5. White dotted lines enclose the PE*
357 *area.* ***(H'')*** *Zoomed region shows the difference between nuclear YAP1-positive cells (yellow*
358 *arrows) and YAP1-negative cells (yellow asterisks). Hoechst signal (blue) highlights cell nuclei.*
359 *YAP1 signal is shown as fire LUT to facilitate the visualization of signal intensity, where blue*
360 *is the minimum and yellow is the maximum. In all graphs, red bars indicate mean ± standard*
361 *deviation.*

362

363 *IFTs interact with YAP1 and regulate its activity.*

364 Taking advantage of cultured cells, we next explored the mechanism by which IFT proteins
365 could regulate YAP1 activity. Immunofluorescence performed in HeLa cells transfected with
366 IFT88-GFP, showed co-localization between IFT88 and YAP1 in the cytoplasm (**Supp. 7 A-**
367 **C**). To confirm a potential physical interaction between IFT proteins with YAP1, we first
368 performed Co-IP experiments using IFT88-GFP and YAP1-Myc in HeLa cells but never
369 obtained any clear interaction. Considering that YAP1 often necessitates the scaffold protein
370 Angiomotin-like 1 (Amotl1) (23), we next performed Co-IP experiment using HA-Amotl1,
371 IFT88-GFP, and YAP1-Myc in HeLa cells. The experiments revealed a clear interaction
372 between YAP1, Amotl1, and IFT88 (**Fig. 4 A**). Similarly, physical interaction between
373 endogenous YAP1, Flag-Amotl1, and IFT20-GFP was observed in transfected HEK293 cells
374 (**Fig. 4 A**). Together, these results reveal that IFT proteins, YAP1, and Amotl1 could function
375 as part of a complex involved in the functional modulation of YAP1 activity *in vivo*.

376 To functionally assess the impact of endogenous IFT88 depletion on YAP1 activity, we next
377 used a DLD-1 IFT88-auxin-inducible degron (AID) cell line, in which a rapid degradation of
378 IFT88 protein can be induced by auxin treatment (**Fig. 4 B**). Of note, DLD-1 cells don't grow
379 cilia allowing us to explore the cytoplasmic, cilia independent function of IFT88 (64).

380 We observed that 2 hours of auxin treatment led to IFT88 and YAP1 degradation. The rapid
381 co-degradation further suggested that both proteins physically interact (**Fig. 4 C**). We confirmed
382 this finding by performing shorter auxin treatments to study the progressive degradation of
383 IFT88 and YAP1 (**Fig. 4 C'**). Importantly, as previously observed *in vivo*, longer depletion of
384 endogenous IFT88 after 6 hours of auxin treatment led to an increase in nuclear YAP1 measured
385 by immunofluorescence (**Fig. 4 D) (Supp. 8 A**). Consistently, the nuclear/cytoplasmic YAP1
386 ratio was also increased (**Supp. 8 A**). Additionally, we confirmed these results using HeLa and

387 MDCK cell lines where IFT88 function was inactivated by IFT88-siRNA. The IFT88-siRNA
388 efficiency was validated by immunofluorescence and western blot (**Supp. 9 A-C**). After 48
389 hours of IFT88-siRNA treatment, nuclear YAP1 signal was measured by immunofluorescence
390 (**Fig. 4 E-F'**). The inactivation of IFT88 was accompanied with increased nuclear YAP1 (**Fig.**
391 **4 E, F**). Altogether, these data indicate that IFT88 can interact with YAP1 in the cytoplasm and
392 is involved in modulating the activation of the Hippo pathway effector YAP1.
393

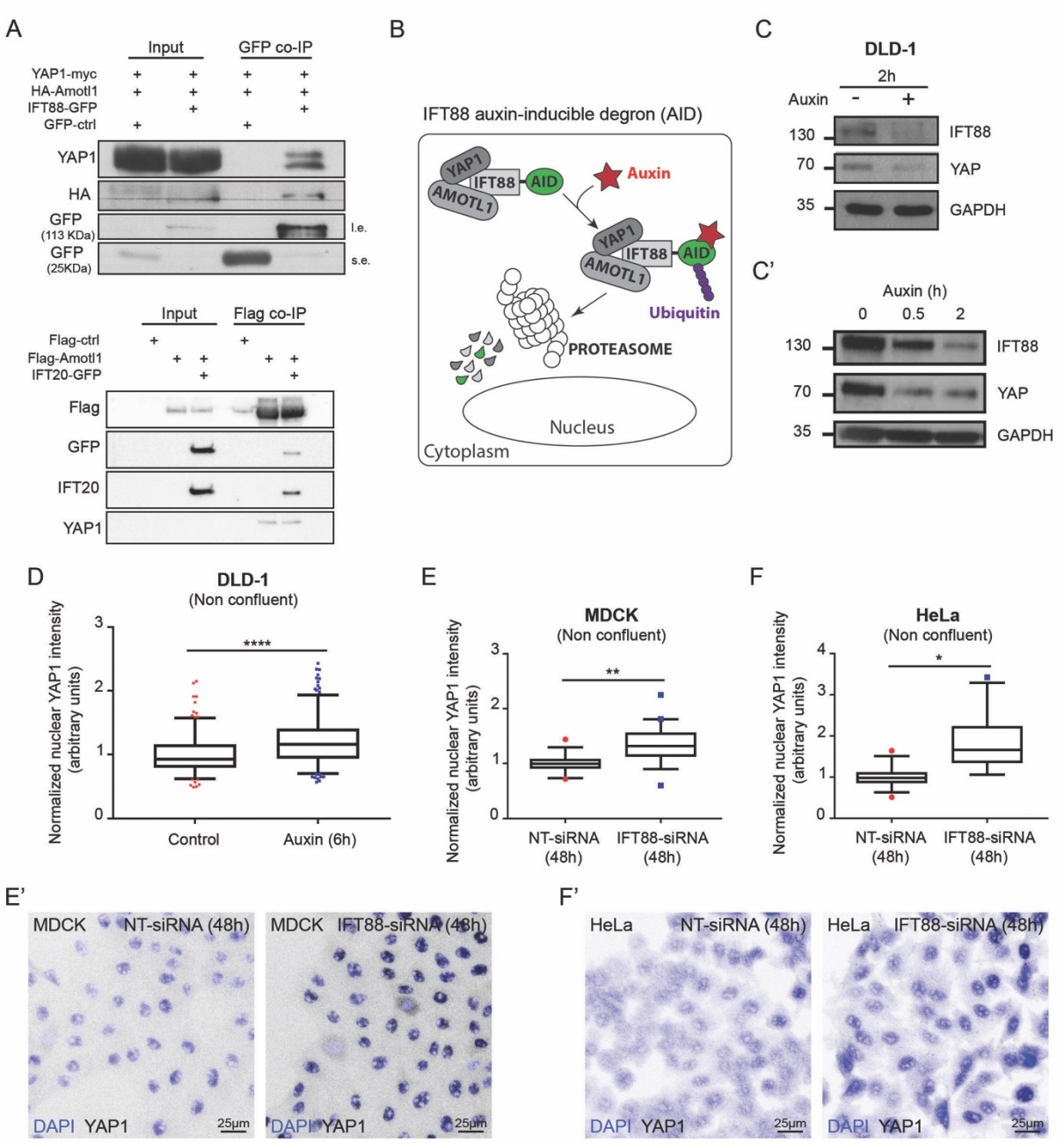

394

395 ***Figure 4. IFT88 and IFT20 are physically associated to YAP1 and IFT88 modulates YAP1***
396 ***activity.***
397 ***(A)*** *Co-IP experiment using HeLa cells transfected with IFT88-GFP, HA-Amotl1 and YAP1-*
398 *Myc. (l.e. = long exposure. s.e. = short exposure). Co-IP experiment using HEK293 cells*
399 *transfected with Flag-Amotl1 and IFT20-GFP. Endogenous levels of Yap1 are monitored.* ***(B)***
400 *Schematic representation of the IFT88 auxin-inducible degron (AID) system* ***(C)*** *Western blot*
401 *analysis of IFT88 AID DLD-1 cells after 2 hours auxin treatment.* ***(C')*** *Western blot analysis*
402 *of IFT88 and YAP1 degradation after auxin treatment (0 h, 0.5h and 2 h).* ***(D)*** *Graph shows the*
403 *increase in normalized YAP1 nuclear signal in cells treated with auxin (6h) (Mann-Whitney p-*
404 *value <0.0001). (controls: 2 replicates, n=204 cells; Auxin 2h: 2 replicates, n=261 cells).* ***(E)***
405 *Graph shows the increase in YAP/WWTR1 (TAZ) nuclear signal in IFT88-siRNA (48h) treated*
406 *MDCK cells (n=5 replicates, average cell number analyzed for each condition = 382, t-test p-*
407 *value 0.004). Box and whiskers (5-95 percentile). Outliers are represented as red dots (NT-*
408 *siRNA) or blue squares (IFT88-siRNA).* ***(E')*** *Immunofluorescence confocal images (z-*
409 *projection) of MDCK cells treated with NT – or IFT88-siRNA (48h). DAPI (blue) and*
410 *YAP/WWTR1 (TAZ) (white inverted LUT).* ***(F)*** *Graph shows the increase in YAP/WWTR1 (TAZ)*
411 *nuclear signal in IFT88-siRNA (48h) treated HeLa cells (n=5 replicates, average cell number*
412 *analyzed for each condition = 252, t-test p-value 0.02). Box and whiskers (5-95 percentile).*
413 *Outliers are represented as red dots (NT-siRNA) or blue squares (IFT88-siRNA).* ***(F')***
414 *Immunofluorescence confocal images (z-projection) of HeLa cells treated with NT – or IFT88-*
415 *siRNA (48h). DAPI (blue) and YAP/WWTR1 (TAZ) (white inverted LUT).*
416
417 To confirm that increased nuclear YAP1 is specific of IFT protein function, we performed
418 IFT88 and IFT20 overexpression assays. While the transfection of pEGFP C1 did not alter the
419 nuclear signal between GFP-positive and GFP-negative cells (endogenous control) (**Supp. 6 D)**

420 **(Supp. 7 B-D**), IFT88-GFP and IFT20-GFP overexpression caused a decrease in nuclear signal
421 (**Supp. 7 C, D**). Together, these data confirm that IFT proteins modulate YAP1 activation.
422
423
424
425 ***Discussion***
426 Primary cilia function has long been implicated in the control of the developmental program,
427 but whether cilia-related proteins could affect cell signaling independently of their ciliary
428 function remains unclear. Here, we have shown that IFT complex B members, IFT88 and IFT20
429 modulate the Hippo pathway effector YAP1 in different cell types. We also demonstrated that
430 IFT88 and IFT20 modulates PE size in mouse and that Ift88 and Ift54 do the same in zebrafish
431 PE and myocardium. Mechanistically, work *in cellulo* suggest that IFT88 physically interacts
432 with YAP1 to modulate its activity. Together, this work establishes a previously unknown role
433 for IFT complex B proteins in regulating cell signaling and tissue growth during cardiogenesis
434 and shed a novel light on cilia related protein function during cardiogenesis.
435 IFT proteins have long been associated with ciliary functions in developmental processes. For
436 example, *ift88* mutants display a number of phenotypes reminiscent of ciliary defects such as
437 abnormal patterning of the neural tube, defects in the Hedgehog pathway and left-right
438 patterning (58). Ift88 has also been associated with planar cell polarity (65) and cell division
439 (15,16). Our observations that the *ift88* mutants show increased number of nuclear Yap1-
440 positive cells in the myocardium and that the *Ift20 KO* mice display increased nuclear
441 Yap1/Amot1 – positive cells in the PE, provide evidences for a novel role of IFT complex B
442 proteins in cardiogenesis. Mechanistically, IFT proteins are best known for their function in
443 ciliary transport (66). Here, we describe an unexpected interaction between the ciliary
444 machinery proteins and a potent mechanosensing pathway, the Hippo pathway. The hippo

445 effector YAP1 is known to have essential roles in cancer (67), regeneration (24,25,68), and
446 organ size control (69–71). Several mechanisms have been shown to regulate the shuttling of
447 YAP1 into the nucleus, including phosphorylation by Hippo kinases. Recent studies show that
448 YAP1 is mechanosensitive and that force applied to the nucleus can directly drive YAP1
449 nuclear translocation (27,72). Additionally, Angiomotin (AMOT) have been shown to interact
450 physically with YAP1 and acts as a buffering factor sequestering YAP1 in the cytoplasm (31).
451 Nevertheless, AMOTL1 has also been shown to co-localize with YAP1 in the nucleus (23,73)
452 demonstrating YAP1 subcellular localization is highly regulated by Motin family proteins. Our
453 results indicate that IFT complex B proteins are also involved in regulating YAP1 localization.
454 We demonstrate that IFT88 interacts biochemically with YAP1 and both co-localize in the
455 cytoplasm. We did not study TAZ, the other Hippo effector which is known to act with YAP1
456 (74) and we cannot draw general conclusions on the role of IFT88 on all the known Hippo
457 effectors. Nevertheless, our work suggests alternative ways to interpret Ift88 mutant phenotypes,
458 which are often interpreted based on polarity or cilia function issues, and, more generally,
459 phenotypes of other mutants with abnormal IFT complex B proteins. Our working model is that
460 Ift88 participates in sequestering YAP1 away from the nucleus using its cargo transport activity.
461 Other cilia related proteins such kinesin2 and IFT complex A proteins have been shown to
462 promote nuclear localization of β-catenin during Wnt signaling in drosophila (75), further
463 suggesting that proteins identified for their ciliary transport functions are not always limited to
464 that function. Interestingly, IFT-A complexes control retrograde protein transport, from the tip
465 to the base of the cilium (76–78), while the IFT-B complexes do the opposite, as observed for
466 YAP1 transport towards the nucleus. Future work will reveal the mechanism by which Ift88
467 limits nuclear translocation of YAP1 in this process and address whether IFT complex A
468 proteins play a role.

469 Importantly, while our study points towards a non-canonical function for IFT complex B
470 proteins, our results do not exclude a role for primary cilia in PE formation. We found that
471 *iguana/dzip* mutants display a avcPE phenotype suggesting that primary cilia function is
472 required for PE morphogenesis. The HH pathway is often associated with ciliary function. To
473 date, a number of studies suggest the proepicardium and epicardium formation are not regulated
474 by Hedgehog signaling (79,80). Indeed, dissection of zebrafish *shha* function in the PE and
475 epicardium using a *tcf21:CreER*, a well-established PE and epicardial tissue driver (81), does
476 not affect PE formation (80). Besides, expression of *Shh*, *Dhh*, *Ihh*, and *Ptch1* was neither
477 detected in the mouse PE nor in the epicardium at subsequent stages (79). Thus, primary cilia
478 certainly operate independently of the HH pathway in the process. Our work further highlights
479 the important role of the BMP pathway in PE formation. BMP is essential for PE formation and
480 morphogenesis (50,82). There is numerous evidence to suggest that primary cilia modulate
481 BMP pathway and, more generally, TGF beta signaling pathways (83,84). In endothelial cells,
482 primary cilia modulate angiogenesis by altering BMP signaling in endothelial cells (85). We
483 speculate the situation is different in PE cells, where BMP is activated downstream of YAP1,
484 and where IFT88 helps to limit YAP1 and BMP signaling. Similarly, secondary heart field
485 development also depends on the modulation of Hippo signaling by BMPs (21).
486 In summary, our study is the first report implicating IFT complex B proteins during PE
487 development by modulating YAP1 activity independently of any cilia function. A deeper
488 understanding of the molecular mechanisms regulating PE development is of great importance,
489 underlined by its role in myocardial maturation and coronary vessel formation during
490 development, as well as the regenerative capacity of the heart (86). Considering that IFT
491 proteins are often associated with ciliopathies, linking IFT with YAP1 activity might have
492 important implications for understanding the etiology of ciliopathies during cardiogenesis and
493 for the interpretation of ciliary defects in IFT mutants.

Acknowledgements

We thank P. Lamperti, E. Steed, A Bhat, D. Riveline, S. Harlepp, J. Godin, A. Benmerah and the Vermot lab for discussion and thoughtful comments on the manuscript, in particular R. Chow for her help with editing. We thank G. Pazour, M. Faucourt and N. Spassky for advice, the gift of plasmids and for providing the *Ift20* and *Ift88* mutant mouse lines and C. Cimper, L. Bombardelli and C. Shea for technical assistance. We are grateful to the IGBMC fish facility, the IGBMC imaging center and the imaging platforms of the SFR Necker. This project has received funding from the European Union's Horizon 2020 research and innovation programme under the Marie Sklodowska-Curie grant agreement No 708312 (MP). This work was supported by FRM (DEQ20140329553), the European seventh framework program (ERC 682938 - EVALVE), ANR (ANR-15-CE13-0015 – liveheart) and by the grant ANR-10-LABX-0030-INRT, a French State fund managed by the Agence Nationale de la Recherche under the frame program Investissements d'Avenir labeled ANR-10-IDEX-0002–02. BD team was supported by ANR-12-CHEX-005 and CNRS. SM team was supported by core funding from the Institut *Imagine*, the Institut Pasteur, the INSERM, the Université Paris Descartes, and a grant from the AFM-Téléthon [Trampoline 18727]. TL was funded by the ED515 (1691/2014).

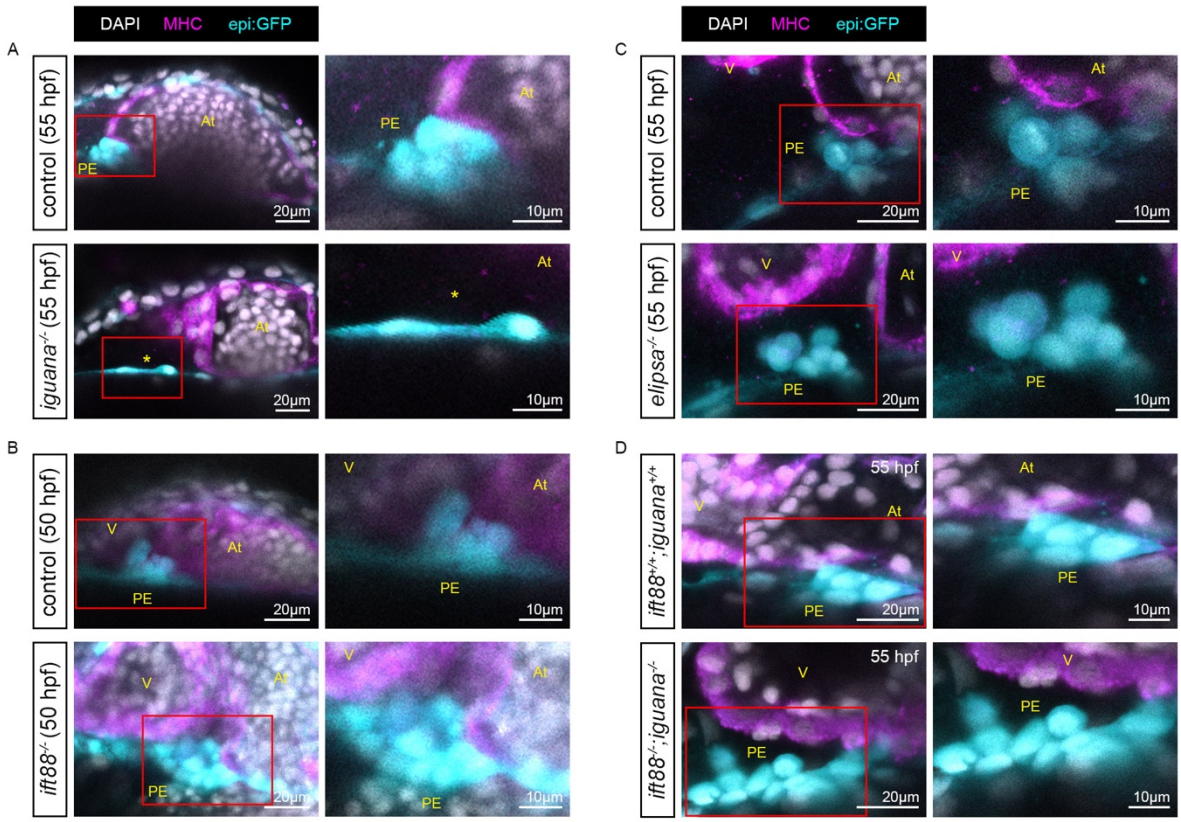

513

514 ***Supplementary Figure 1. IFT complex B mutants show increased proepicardial size in***

515 ***zebrafish.***

516 ***(A)*** *Confocal sections of whole mount immunofluorescence of iguana$^{-/-}$, epi:GFP and control*

517 *using anti-myosin heavy chain antibody (MHC) (magenta), anti-GFP (cyan) and DAPI (white)*

518 *antibodies at 55 hpf. Asterisk shows lack of avcPE as there is only one rounded PE cell.* ***(B)***

519 *Confocal sections of whole mount immunofluorescence of ift88$^{-/-}$, epi:GFP and control using*

520 *anti-myosin heavy chain antibody (MHC) (magenta), anti-GFP antibody (cyan) and DAPI*

521 *(white) at 50 hpf.* ***(C)*** *Confocal sections of whole mount immunofluorescence of elipsa$^{-/-}$,*

522 *epi:GFP and control using anti-myosin heavy chain antibody (MHC) (magenta), anti-GFP*

523 *(cyan) and DAPI (white) antibodies at 55 hpf.* ***(D)*** *Confocal sections of whole mount*

524 *immunofluorescence of ift88$^{-/-}$, iguana$^{-/-}$, epi:GFP and ift88$^{+/+}$, iguana$^{+/+}$, epi:GFP using anti-*

525 *myosin heavy chain antibody (MHC) (magenta), anti-GFP (cyan) and DAPI (white) antibodies*

526 *at 55 hpf. All images are ventral views, anterior is to the top. V, ventricle; At, atrium; PE,*

527 *avcPE. Zoomed regions contained inside the red boxes are showed on the right side.*

528

529

530

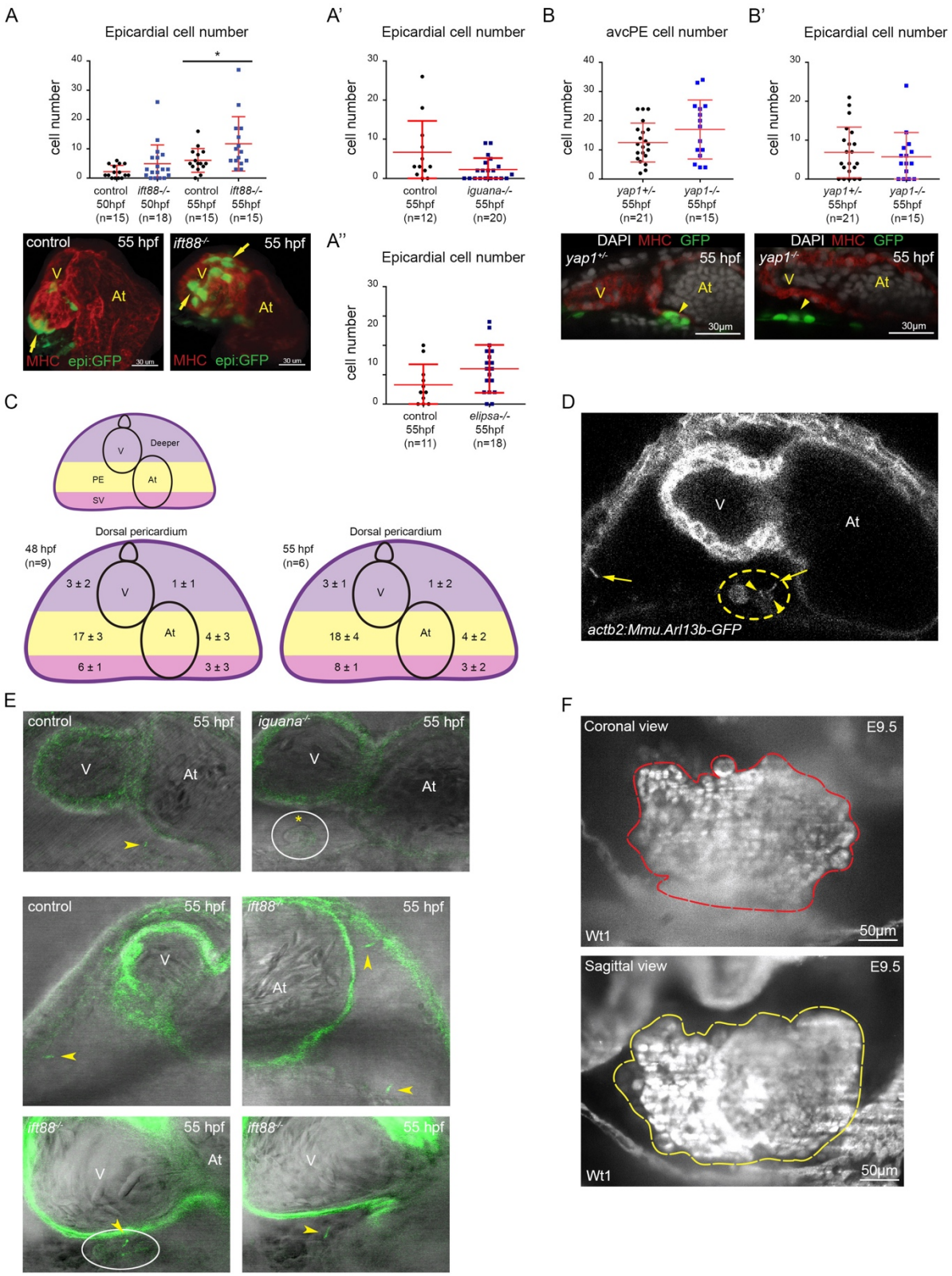

531

532 ***Supplementary Figure 2. Cilia protruding into the pericardial cavity are distributed***

533 ***heterogeneously in zebrafish during proepicardial development.***

534 ***(A-A'')*** *Graphs show epicardial cell numbers quantified in ift88, iguana and elipsa mutants in*
535 *epi:GFP background.* ***(A)*** *At 55 hpf, ift88 mutants (n=15) showed increased epicardial cell*
536 *numbers (t-test p value 0.04). 3D projections of whole mount immunofluorescence of hearts*
537 *using anti-myosin heavy chain antibody (red) and GFP (green) expression. Ventral view,*
538 *anterior is to the top. Arrows mark some epicardial cells;* ***(A')*** *iguana mutants (n=20) showed*
539 *a tendency towards decreased epicardial cell numbers (t-test p value 0.055), while* ***(A'')*** *elipsa*
540 *mutants (n=18) showed a tendency towards increased epicardial cell number (t-test p value*
541 *0.08).* ***(B)*** *Graph shows avcPE cell numbers quantified in yap1$^{-/-}$ (n=15) and control (n=21)*
542 *embryos in tcf21:nsl-GFP background at 55 hpf. (t-test p-value 0.12) Control and yap1$^{-/-}$*
543 *immunofluorescence confocal sections labelled with anti-myosin heavy chain antibody (MHC)*
544 *(red), GFP (green), DAPI (white). Ventral view, anterior is to the top. Yellow arrowheads point*
545 *at the avcPE.* ***(B')*** *Graph shows epicardial cell numbers quantified in yap1$^{-/-}$ (n=15) and*
546 *control (n=21) embryos in tcf21:nsl-GFP background at 55 hpf. (Mann Whitney p-value 0.63)*
547 ***(C)*** *For cilia quantification, we divided the dorsal pericardial wall in to three different regions:*
548 *SV region, including the sinus venosus (pink); PE region, where the avcPE forms (yellow) and*
549 *Deeper region (purple). These three regions were subdivided in to right and left halves,*
550 *containing the ventricle or the atrium respectively. At 48 hpf (n=9 larvae), prior to PE*
551 *formation, cilia protruding from the dorsal pericardium showed a heterogeneous distribution.*
552 *Interestingly, the right half of the SV (6 ± 1) and the PE (17 ± 3) regions, where both PE clusters*
553 *will form, presented higher cilia number than the rest of the regions. At 55 hpf, when the avcPE*
554 *is formed, the cilia distribution was similar to that observed at 48 hpf (n= 6 larvae).* ***(D)***
555 *Confocal section of actb2:Mmu.Arl13b-GFP embryo (55 hpf). Yellow dotted circle encloses the*
556 *avcPE. Yellow arrows point to cilia protruding from the ventral and dorsal pericardium. Yellow*
557 *arrowheads point at immotile and bent cilia protruding from a few avcPE cells.* ***(E)*** *Confocal*
558 *section of iguana; actb2:Mmu.Arl13b-GFP and control embryos (55 hpf). Yellow arrowhead*

points at cilium protruding from the avcPE. Yellow asterisk shows lack of cilia in the avcPE (enclosed in the white circle). Confocal section of ift88; actb2:Mmu.Arl13b-GFP and control embryos (55 hpf). In control embryo, yellow arrowhead points at cilium protruding from the ventral pericardium. In ift88 mutant embryo, yellow arrowheads point at cilia protruding from ventral and dorsal pericardium and the avcPE (enclosed in the white circle). ***(F)*** *Coronal and sagittal sections acquired by light sheet microscopy to illustrate the methods used to measure PE volume (labeled with anti-Wt1 antibody). Red and yellow dotted shapes enclose the PE area. In all images ventral views, anterior is to the top. V, ventricle; At, atrium. In all graphs, red bars indicate mean ± standard deviation.*

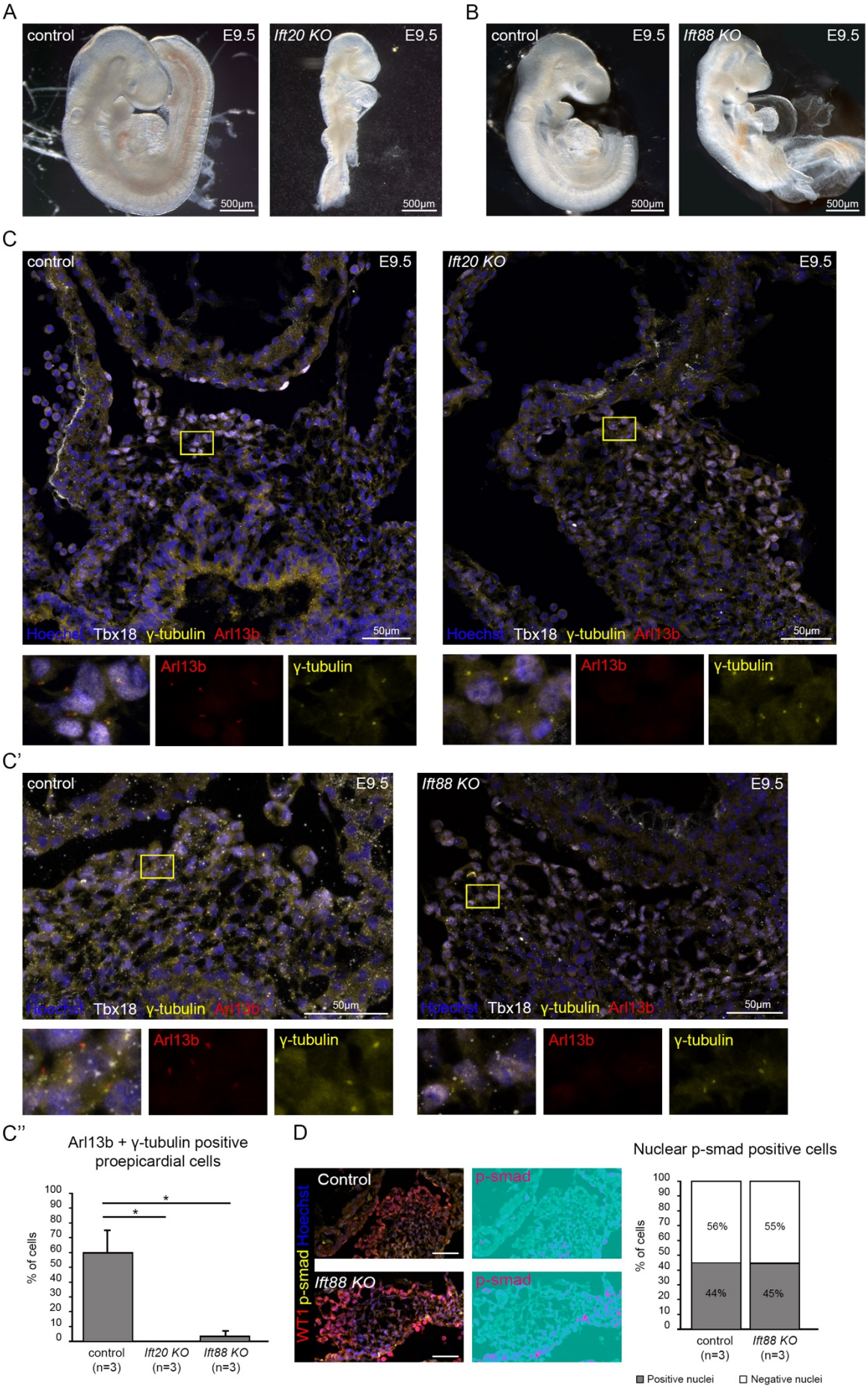
A
control
E9.5
Ift20 KO
E9.5
500µm
B
control
E9.5
Ift88 KO
E9.5
500µm
C
control
E9.5
Ift20 KO
E9.5
Hoechst Tbx18 γ-tubulin Arl13b
50µm
Arl13b
γ-tubulin
C'
control
E9.5
Ift88 KO
E9.5
Hoechst Tbx18 γ-tubulin Arl13b
50µm
Arl13b
γ-tubulin
C''
Arl13b + γ-tubulin positive proepicardial cells
% of cells
control (n=3)
Ift20 KO (n=3)
Ift88 KO (n=3)
D
Control
p-smad
Ift88 KO
WT1 p-smad Hoechst
Nuclear p-smad positive cells
% of cells
56%
44%
55%
45%
control (n=3)
Ift88 KO (n=3)
Positive nuclei
Negative nuclei

569

570 ***Supplementary Figure 3. Ift20 KO mice proepicardial cells lack cilia.***

571 ***(A,B)*** *Ift20 and Ift88 KO mice show left-right patterning defects including heart looping defects*
572 *at E9.5.* ***(C)*** *Control and Ift20 KO cryosections imaged by confocal microscopy after labelling*
573 *with anti-TBX18 (white), anti-Arl13b (red) and anti-γ-tubulin (yellow) antibodies and Hoechst*
574 *(blue) at E9.5. Zoomed region (enclosed in yellow box) shows the lack of Arl13b signal in Ift20*
575 *KO mice. Individual channels are shown for Arl13b (red), γ-tubulin (yellow).* ***(C')*** *Control and*
576 *Ift88 KO cryosections labelled with anti-TBX18 (white), anti-Arl13b (red) and anti-γ-tubulin*
577 *(yellow) antibodies and Hoechst (blue) at E9.5. Zoomed region (enclosed in yellow box) shows*
578 *the decrease of Arl13b signal in Ift88 KO mice. Individual channels are shown for Arl13b (red),*
579 *γ-tubulin (yellow).* ***(C'')*** *Graph shows the percentage of ciliated PE cells in Ift20 KO (n=3,*
580 *Ift88 KO (n=3) and control (n=3) mice. The percentage of ciliated PE cells is severely reduced*
581 *in Ift20 KO (n=3) and Ift88 KO (n=3) when compared to control (n=3) mice. (t-test Ift20 p-*
582 *value 0.024; t-test Ift88 p-value 0.025)* ***(D)*** *Control and Ift88 KO cryosections labelled with*
583 *WT1 (red), p-smad 1/5/9 (yellow) and Hoechst (blue) at E9.5. Individual channel is displayed*
584 *for p-smad 1/5/9 as ice LUT to facilitate the visualization of signal intensity (green is the*
585 *minimum and red is the maximum).Graph shows that the percentage of p-smad 1/5/9 positive*
586 *PE cells is similar in Ift88 KO (n=3 embryos: 1477 nuclei analyzed) and controls (n=3 embryos:*
587 *1514 nuclei analyzed) (Chi-square test* of homogeneity *=0.15225, p-value 0.6964 on 1 degree*
588 *of freedom).*

589

590

591

592

593

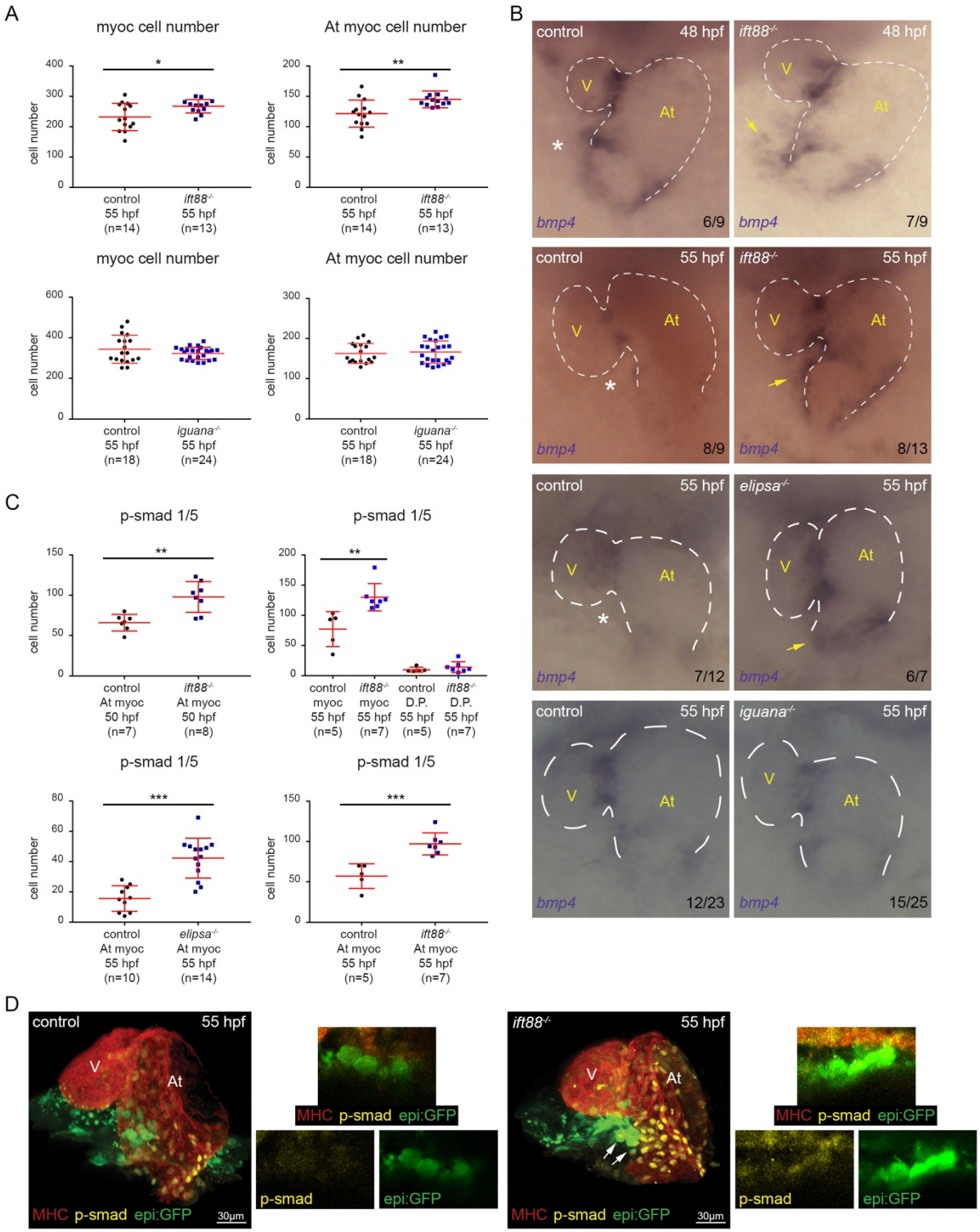

594

595 ***Supplementary Figure 4. bmp4 is overexpressed in ift88, elipsa/ift54 and Ift20 mutants.***

596 ***(A)*** *The top two graphs show total myocardial and atrial-myocardial cell numbers quantified*

597 *in ift88 (n=13) mutants and controls (n=14) at 55 hpf. (t-test total myocardium p-value 0.016;*

598 *atrial myocardium p-value 0.003). The bottom two graphs show total myocardial and atrial-*

599 *myocardial cell number quantified in iguana (n=24) mutants and controls (n=18) at 55 hpf. (t-*
600 *test total myocardium p-value 0.2; atrial myocardium p-value 0.68).* ***(B)*** *Whole mount bmp4 in*
601 *situ hybridization performed on control and ift88 mutant embryos at 48 hpf and at 55 hpf on*
602 *ift88, elipsa and iguana mutants and their controls. Yellow arrows point to bmp4*
603 *overexpression, while white asterisks mark reduced or absent expression. Ventral views,*
604 *anterior is to the top. V, ventricle; At, atrium.* ***(C)*** *Graphs show number of p-smad1/5 positive*
605 *cells in the atrial myocardium quantified in ift88 (at 50 hpf n=8; at 55 hpf n=7), elipsa (n=14)*
606 *mutants and their controls (n=7; n=5; n=10 respectively). At 50 hpf, ift88 mutants show p-*
607 *smad 1/5 increased cell number on the atrial myocardium (t-test p value 0.0017). Similar data*
608 *were obtained at 55 hpf (t-test p value 0.0008). At 55 hpf, elipsa mutants also show p-smad 1/5*
609 *increased cell number in the atrial myocardium (t-test p value 0.0003). At 55 hpf, ift88 mutants*
610 *show p-smad 1/5 increased cell numbers in the myocardium (t-test p value 0.005).* ***(D)*** *3D*
611 *projections of whole mount immunofluorescence of hearts using anti-myosin heavy chain*
612 *antibody (MHC) (red), epi:GFP (green) and anti-p-smad1/5 (yellow) antibody. Arrows mark*
613 *avcPE cells positive for epi:GFP and p-smad1/5. Zoomed confocal sections show avcPE in*
614 *ift88 mutant and control embryos. Individual channels are displayed for p-smad 1/5 and GFP.*
615 *Ventral views, anterior is to the top. In all graphs, red bars indicate mean ±standard deviation.*

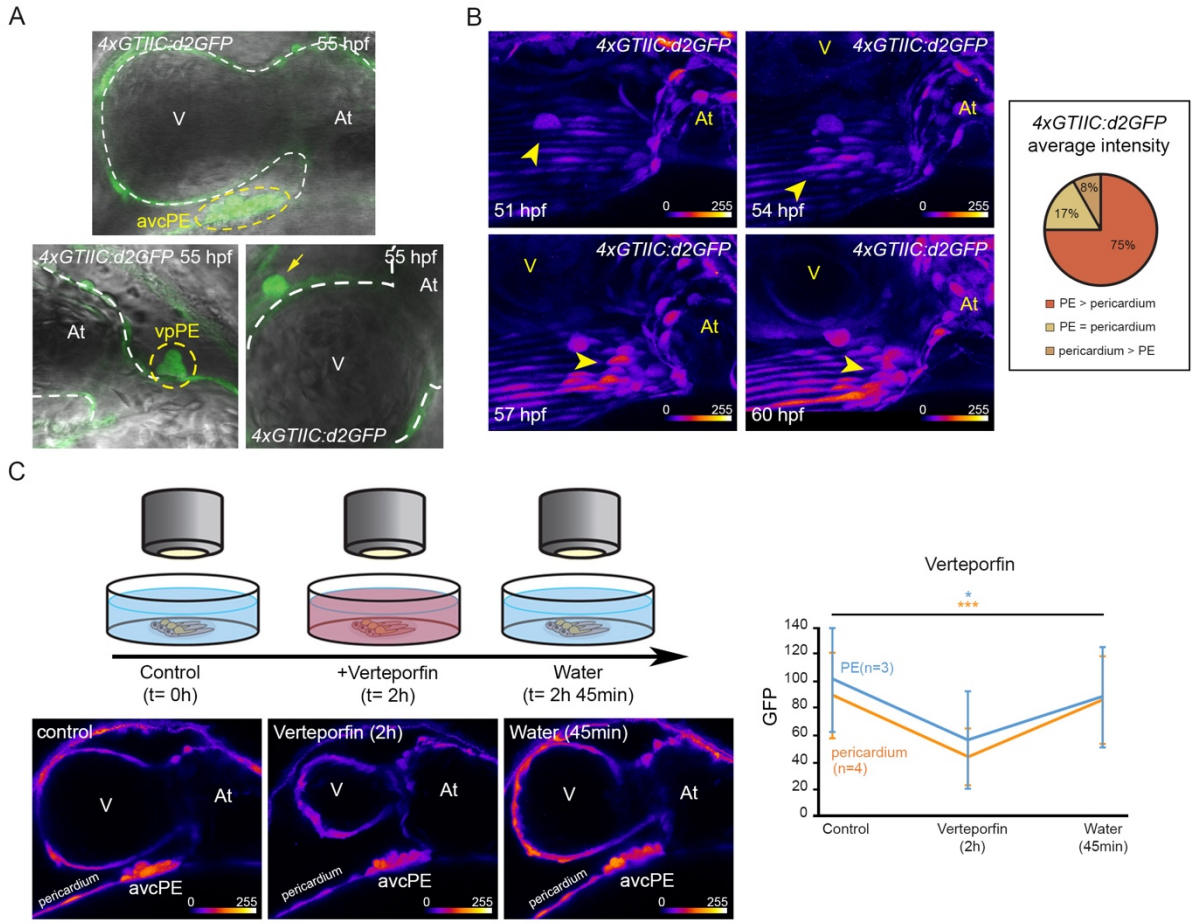

Supplementary Figure 5 Yap1-Tead activity during proepicardial development in zebrafish. ***(A)*** *Confocal sections of 4xGTIIC:d2GFP signal merged with bright-field, showing Yap/Wwtr1-Tead interaction in avcPE, vpPE, epicardial, myocardial and pericardial cells (n=12). Yellow dashed circles enclose the avcPE and the vpPE. Arrow shows an epicardial cell. Ventral views, anterior is to the top.* ***(B)*** *Maximum projection 4xGTIIC:d2GFP time lapse (51-60 hpf) snapshots (n=6). Arrowheads point at the avcPE. GFP signal is shown as fire LUT where blue is the minimum and yellow is the maximum to facilitate visualization of the intensity changes through the experiment. Ventral views, anterior is to the top. V, ventricle; At, atrium. Graph shows 75% of the embryos displayed higher average GFP intensity in PE cells than in pericardial cells (n=12, 7-15 cells of each type).* ***(C)*** *Scheme of the experiment to assess Verteporfin specificity. Time lapse performed on 4xGTIIC:d2GFP embryos at 55 hpf. Yap/Wwtr1-Tead activity (average GFP intensity) was measured on the same PE (3 cells in*

629 *each embryo, n=3) and pericardial (3 cells in each embryo, n=4) cells at three timepoints:*
630 *before adding Verteporfin (5µM) (t=0h), after 2 hours of treatment (t=2h) and 45 min after*
631 *washing out the Verteporfin with fish water (t=2h45 min). Graph shows the decrease in*
632 *Yap/Wwtr1-Tead activity (average GFP intensity) due to Verteporfin treatment on PE (blue)*
633 *and pericardial (orange) cells, which is rescued after removing the inhibitor. (Pericardial cells*
634 *ANOVA p value 0.0007. PE cells ANOVA p value 0.05). Example of 4xGTIIC:d2GFP embryo*
635 *confocal sections used for the experiment. GFP signal is shown as fire LUT where blue is the*
636 *minimum and yellow is the maximum to facilitate visualization of the intensity changes through*
637 *the experiment. Ventral views, anterior is to the top. V, ventricle; At, atrium.*

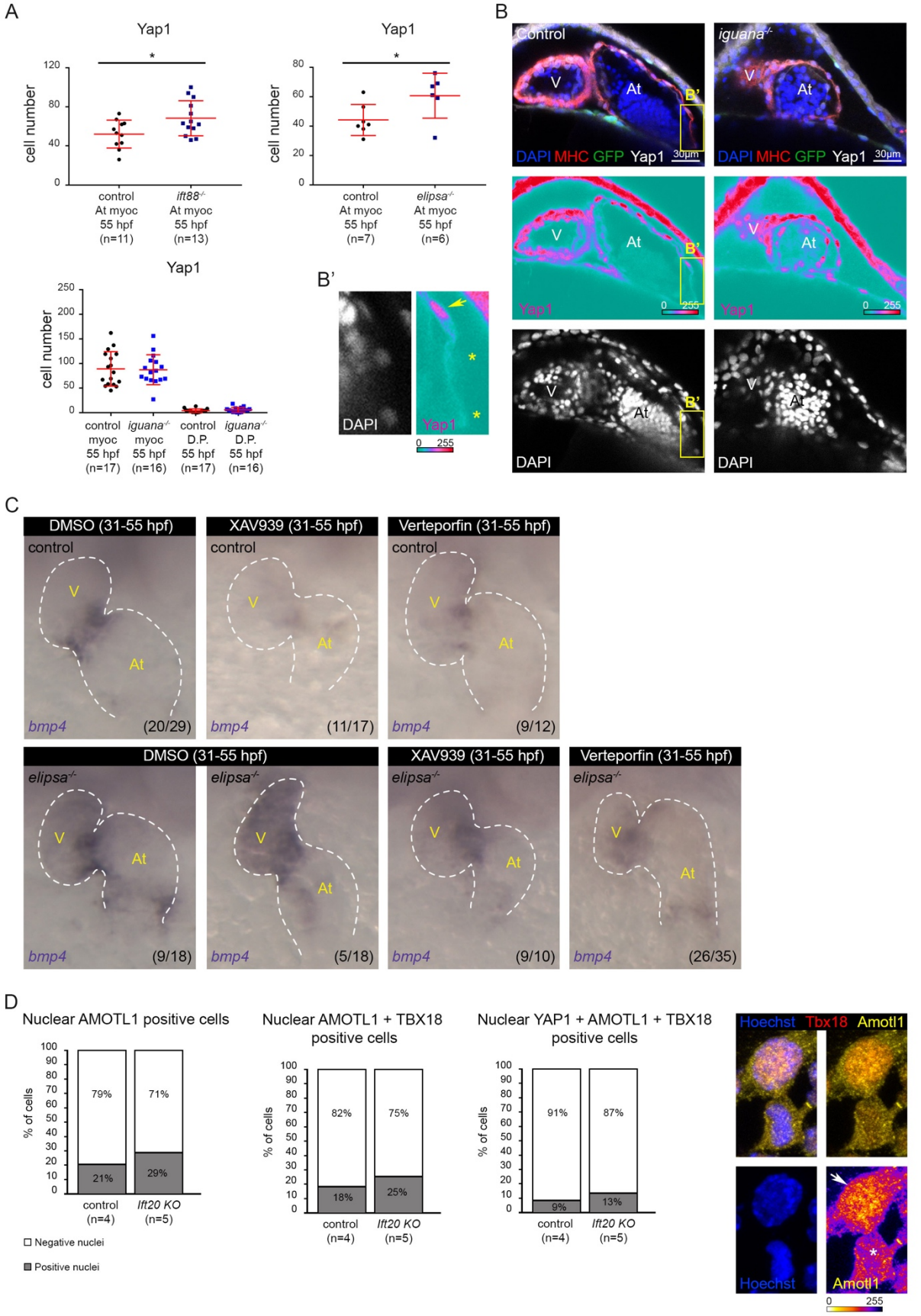
A
Yap1
cell number
control At myoc 55 hpf (n=11)
ift88-/- At myoc 55 hpf (n=13)
control At myoc 55 hpf (n=7)
elipsa-/- At myoc 55 hpf (n=6)
control myoc 55 hpf (n=17)
iguana-/- myoc 55 hpf (n=16)
control D.P. 55 hpf (n=17)
iguana-/- D.P. 55 hpf (n=16)
B'
DAPI
Yap1
B
Control
iguana-/-
V
At
B'
DAPI MHC GFP Yap1
30µm
C
DMSO (31-55 hpf)
XAV939 (31-55 hpf)
Verteporfin (31-55 hpf)
control
elipsa-/-
bmp4
(20/29)
(11/17)
(9/12)
(9/18)
(5/18)
(9/10)
(26/35)
D
Nuclear AMOTL1 positive cells
Nuclear AMOTL1 + TBX18 positive cells
Nuclear YAP1 + AMOTL1 + TBX18 positive cells
% of cells
79%
21%
71%
29%
82%
18%
75%
25%
91%
9%
87%
13%
control (n=4)
Ift20 KO (n=5)
Negative nuclei
Positive nuclei
Hoechst Tbx18 Amotl1
Hoechst
Amotl1
0 255

638

639 ***Supplementary Figure 6. Yap1 activity is increased in the myocardium of ift88 and***
640 ***elipsa/ift54 zebrafish mutants and AMOTL1 activity is increased in IFT20 KO mice***
641 ***proepicardium***

642 ***(A)*** *The top two graphs show number of Yap1-positive cells in the atrial myocardium quantified*
643 *in ift88$^{-/-}$, epi:GFP (n=13) and elipsa$^{-/-}$, epi:GFP (n=6) mutants and their controls (n=11 and*
644 *n=7 respectively) at 55 hpf. Mutants show increased Yap1-positive cell numbers (t-test ift88 p*
645 *value 0.024 and elipsa p value 0.042). Bottom graph shows number of Yap1-positive cells in*
646 *the myocardium and dorsal pericardium (D.P.) quantified in iguana$^{-/-}$, epi:GFP (n=16) mutants*
647 *and their controls (n=17) at 55 hpf (t-test myocardium p value 0.875 and D.P. p value 0.312).*
648 ***(B)*** *Control and iguana$^{-/-}$, epi:GFP immunofluorescence confocal sections labelled with anti-*
649 *myosin heavy chain antibody (MHC) (red), GFP (green), anti-Yap1 antibody (white) and DAPI*
650 *(blue) at 55 hpf. Individual channel is displayed for Yap1 (signal is shown as ice LUT to*
651 *facilitate visualization of signal intensity, where green is the minimum and red is the maximum)*
652 *and DAPI (white). Ventral view, anterior is to the top.* ***(B')*** *Zoomed region (yellow box in panel*
653 ***B****) shows Yap1 and DAPI channels to illustrate the method used to quantify Yap1-positive (Yap1*
654 *signal in the nucleus: yellow arrow) and –negative (yellow asterisks) cells.* ***(C)*** *Whole mount*
655 *bmp4 in situ hybridization in untreated elipsa mutant (n=18) and control (n=29) embryos and*
656 *treated with XAV939 (10μM) (elipsa mutant, n=10 and control, n=17) or Verteporfin (20μM)*
657 *(elipsa mutant, n=35 and control, n=12) from 31 to 55 hpf. Treated embryos showed either*
658 *decreased or absent bmp4 expression at the atrioventricular canal myocardium and the venous*
659 *pole. Ventral views, anterior is to the top.* ***(D)*** *Graphs show the percentages of AMOTL1-*
660 *positive PE cells, double AMOTL1-TBX18-positive PE cells and triple YAP1- AMOTL1-*
661 *TBX18-positive PE cells in Ift20 KO (n=5 embryos: 1196 nuclei analyzed) and control (n=4*
662 *embryos: 929 nuclei analyzed) mice at E9.5. The percentage of nuclear AMOTL1-positive cells*
663 *(Chi-square test* of homogeneity *= 14,748, p-value 1,23E-04 on 1 degree of freedom), nuclear*

AMOTL1-TBX18-positive cells (Chi-square test of homogeneity *= 12,506, p-value 4,06E-04 on 1 degree of freedom) and nuclear YAP1-AMOTL1-TBX18-positive cells (Chi-square test* of homogeneity *= 6,9059, p-value 8,59E-03 on 1 degree of freedom) were higher in Ift20 KO than in control mice. Control (n=4) and Ift20 KO (n=5) sections labelled with TBX18 (red), Amotl1 (yellow) and Hoechst (blue). Individual AMOTL1 channel shows the difference between nuclear AMOTL1-positive cells (white arrow) and AMOTL1-negative cells (white asterisk). AMOTL1 signal is shown as fire LUT to facilitate visualization of the signal intensity, where blue is the minimum and yellow is the maximum. In all graphs, red bars indicate mean ±standard deviation. V, ventricle; At, atrium.*

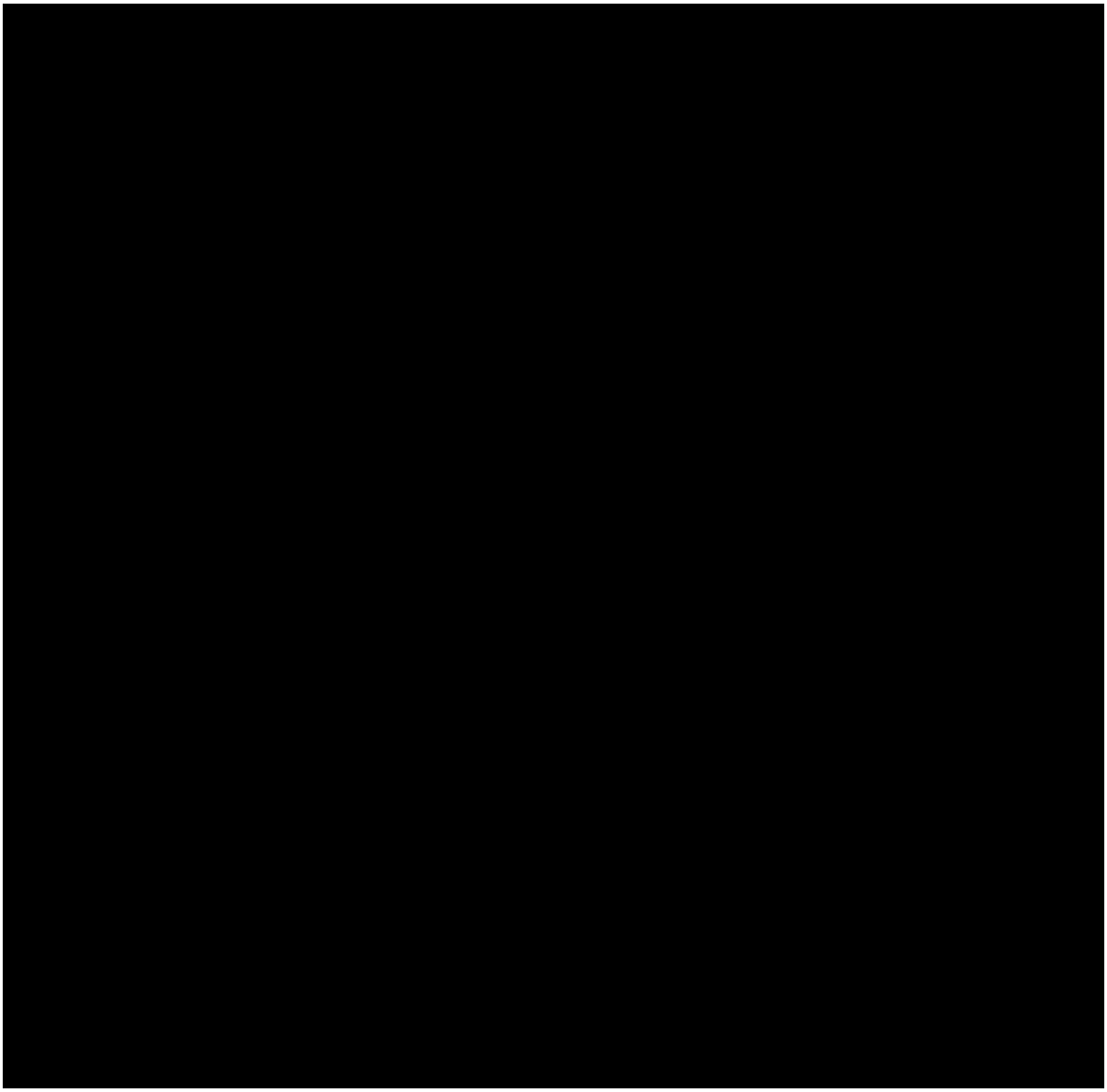

Supplementary Figure 7. IFT88-GFP co-localize with YAP1 in the cytoplasm.

(A) *Confocal section of HeLa cells transfected with IFT88-GFP and Yap1-Myc plasmids (48h). DAPI (blue), IFT88-GFP (green) and Yap1 (visualized using anti-Myc antibody) (red). Individual channels are displayed for IFT88-GFP and Yap1-Myc.* ***(1-4)*** *Zoom of selected areas inside boxes showing co-localization.* ***(B)*** *Confocal sections of HeLa cells transfected with IFT88-GFP (48h) showing co-localization with endogenous YAP (visualized using anti-YAP/WWTR1 (TAZ) antibody). DAPI (blue), IFT88-GFP (green) and YAP1 (magenta).* ***(1-3)*** *Zoom of the selected areas inside white boxes showing co-localization of IFT88 and YAP1. Individual channels are displayed for IFT88-GFP and YAP1 signals.* ***(C)*** *Confocal sections of*

684 *HeLa cells transfected with Yap1-Myc (48h) showing co-localization with endogenous YAP1*
685 *(visualized using anti-YAP/WWTR1 (TAZ) antibody). DAPI (blue), Yap1-Myc (green) and*
686 *YAP1 (magenta).* ***(1-3)*** *Zoom of the selected areas inside white boxes showing examples of co-*
687 *localization between Yap1-Myc (visualized using anti-Myc antibody) and endogenous YAP1*
688 *(using YAP/WWTR1 (TAZ) antibody) signals. Individual channels are displayed for Yap1-Myc*
689 *and YAP1 signals.* ***(D)*** *Confocal sections of HeLa cells transfected with pEGFP C1 (48h) do*
690 *not show co-localization with endogenous YAP1 (visualized using anti-YAP/WWTR1 (TAZ)*
691 *antibody). DAPI (blue), pEGFP C1 (green) and YAP1 (magenta). Individual channels are*
692 *displayed for pEGFP C1 and YAP1 signals.*

Supplementary Figure 8. IFT88 and IFT20 regulate YAP1 activity.

(A) *YAP1 Nuclear/cytoplasmic ratio is increased in cells treated with auxin (6h) (Mann-Whitney p-value 0.004). (controls: 2 replicates, n=102 cells; Auxin 6h: 2 replicates, n=104 cells). Immunofluorescence confocal images (z-projection) of DLD-1 cells treated with auxin (6 h) and controls. DAPI (blue), YAP1 (white) and α-tubulin (red). Zoomed regions show DAPI and YAP1 channels. YAP1 channel is shown in ice LUT where green is the minimum and red is the maximum to facilitate the visualization of signal intensity increases after treatment.* ***(B-D)***

701 *IFT88 and IFT20 overexpression assays performed in HeLa cells (48h). Graphs show nuclear*
702 *YAP/WWTR1 (TAZ) signal in GFP-positive cells (+ GPF), compared to GFP-negative cells (-*
703 *GPF: endogenous control) in cells transfected with pEGFP C1 (GFP control) (n=4 replicates,*
704 *average cell number analyzed for each condition = 22, t-test p-value 0.5)* ***(B)****, IFT88-GFP (n=3*
705 *replicates, average cell number analyzed for each condition = 23, t-test p-value 0.01)* ***(C)*** *or*
706 *IFT20-GFP (n=4 replicates, average cell number analyzed for each condition = 27, t-test p-*
707 *value 0.03)* ***(D)****. Box and whiskers (5-95 percentile). Outliers are represented as red dots (-*
708 *GFP) or blue squares (+GFP). Immunofluorescence confocal images (z-projection) of cells*
709 *transfected with pEGFP C1 (GFP control), IFT88-GFP or IFT20-GFP. DAPI (blue) and*
710 *YAP/WWTR1 (TAZ) (white). Yellow arrows mark GFP signal.*
711
712
713
714
715
716
717

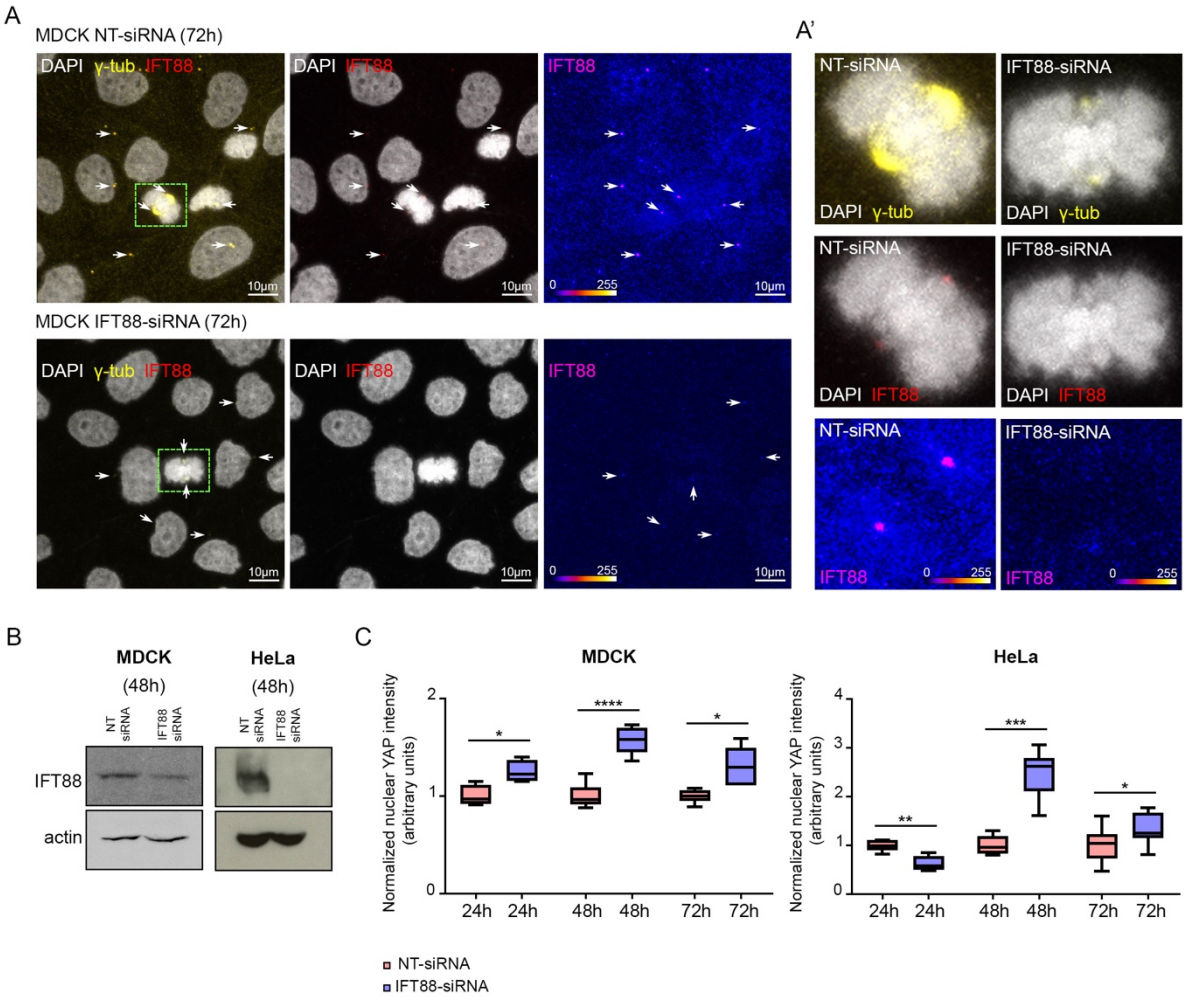

Supplementary Figure 9. Efficiency validation of IFT88-siRNA in MDCK and HeLa cells. ***(A)*** *Immunofluorescence microscopy images (maximum projection) of MDCK cells treated with NT- or IFT88-siRNA (72h). DAPI (white), γ-tubulin (yellow) and IFT88 (red). White arrows highlight IFT88-positive centrosomes facilitating the visualization of IFT88 signal depletion upon IFT88-siRNA treatment.* ***(A')*** *Zoom of dividing cells (green boxes) treated with NT-siRNA and IFT88-siRNA respectively. Centrosomes show reduced IFT88 (red) and γ-tubulin (yellow) signal after IFT88 depletion. DAPI (white). IFT88 channel is shown in fire LUT where blue is the minimum and yellow is the maximum to facilitate the visualization of the intensity reduction after the treatment.* ***(B)*** *Western blot analysis of HeLa and MDCK cells after 48h NT- and IFT88-siRNA treatments respectively.* ***(C)*** *Graphs show the increase in nuclear YAP/WWTR1 (TAZ) signal in IFT88-siRNA treated cells (blue), compared to NT-siRNA controls (red) at 24,*

730 *48 and 72h. Box and whiskers (5-95 percentile). (MDCK: 24h: n=1 replicate, average cell*
731 *number analyzed for each condition = 42, t-test p-value 0.02; 48h: n=1 replicate, average cell*
732 *number analyzed for each condition = 52, t-test p-value <0.0001; 72h: n=1 replicate, average*
733 *cell number analyzed for each condition = 126, t-test p-value 0.01) (HeLa: 24h: n=1 replicate,*
734 *average cell number analyzed for each condition = 12, t-test p-value 0.001; 48h: n=1 replicate,*
735 *average cell number analyzed for each condition = 12, t-test p-value 0.0002; 72h: n=1 replicate,*
736 *average cell number analyzed for each condition = 32, t-test p-value 0.047).*
737
738
739

Average intensity	Embryo_01	Embryo_02	Embryo_03	Embryo_04	Embryo_05	Embryo_06
PE cells	71,37	72,42	30,84	89,57	69,72	49,63
St-Dev	11,91	21,49	26,85	20,56	24,85	13,35
Pericardial cells	52,45	45,17	55,81	94,08	49,98	29,95
St-Dev	21,16	9,76	18,25	29,84	14,67	7,51
t-test	**0,0325**	**0,0084**	0,0101	0,7309	0,0608	**0,0001**

Average intensity	Embryo_07	Embryo_08	Embryo_09	Embryo_10	Embryo_11	Embryo_12
PE cells	63,69	60,99	115,45	64,67	56,23	107,03
St-Dev	26,92	18,28	6,52	11,43	10,46	21,14
Pericardial cells	28,76	31,59	74,03	36,44	30,05	68,40
St-Dev	16,68	7,78	22,14	6,82	8,85	28,52
t-test	**0,0055**	**0,0005**	**0,0001**	**0,0000**	**0,0002**	**0,0024**

740

741 ***Supplementary Table 1. Yap/Wwtr1-Tead activity (GFP average intensity) in PE and***
742 ***pericardial cells.***
743
744 ***Movie 1. Multiple avcPE clusters in ift88 mutant.***
745
746 ***Movie 2. Immotile and bent cilia protruding from the avcPE.***
747
748 ***Movie 3. Absence of avcPE cluster in iguana mutant.***
749
750 ***Movie 4. Yap/Wwtr1-Tead activity during avcPE development (51-60 hpf).***
751
752 ***Movie 5. 3D projection of the PE (marked by anti-Wt1 antibody) of a control embryo at E***
753 ***9.5.***
754
755 ***Movie 6. 3D projection of the PE (marked by anti-Wt1 antibody) of a IFT20 KO embryo at E***
756 ***9.5.***
757
758
759

760 ***Material and Methods***

761 *Zebrafish (ZF) husbandry and embryo treatments:*

762 Animal experiments were approved by the Animal Experimentation Committee of the
763 Institutional Review Board of the IGBMC. ZF lines used in the study were *Et(-26.5Hsa.WT1-*
764 *1gata2:EGFP)*^{cn1} transgenic line (referred to as *epi:GFP*) (46), *amotl2a* ^{fu46} (33), *elipsa* ^{tp49d}
765 (10), *ift88* $^{tz288/oval}$ (53), *iguana* ^{ts294e} (54), *yap1* ^{fu48} (33), *4xGTIIC:d2GFP*
766 (61),*actb2:Mmu.Arl13b-GFP* (56) and *tcf21:NLS-EGFP* (87). All animals were incubated at
767 28.5°C for 24h before treatment with 1-phenyl-2-thiourea (PTU) (Sigma Aldrich) to prevent
768 pigment formation.

769 Verteporfin (Sigma Aldrich) was diluted to 5 µM in fish tank water with 0.0033% PTU, in
770 which larvae were incubated in darkness for 5h at 28.5°C.

771 *ZF Immunofluorescence:*

772 Embryos were fixed at the desired stages in 4% paraformaldehyde (PFA) overnight at 4°C.
773 After washing in 0.1% PBS Tween 20, embryos were permeabilized in 0.5% PBS Triton X-100
774 for 20 min at room temperature (RT). Samples were washed and then blocked (3% albumin
775 from bovine serum (BSA), 5% goat serum, 20 mM MgCl2, 0.3% Tween 20 in PBS) during 2h
776 at RT. Primary antibodies were added in the blocking solution and incubated overnight at 4°C.
777 Secondary antibodies were added in 0.1% PBS Tween20 after thorough washing and incubated
778 overnight at 4°C. Embryos were washed and incubated with DAPI (Invitrogen), 1:1000, for 15
779 min at RT. After being thoroughly washed, samples were mounted for imaging on a Leica SP8
780 confocal with a dipping immersion objective (Leica HCX IRAPO L, 25X, N.A. 0.95). Z-stacks
781 were taken every 10 µm. 3D images were reconstructed using IMARIS software (Bitplane
782 Scientific Software). The ventral pericardium was digitally removed to provide a clearer view
783 of the heart.

784 Antibodies used were as follows: anti-myosin heavy chain (MF20, DSHB) 1:20, anti-GFP
785 (AVES) 1:500, anti-phospho-Smad 1/5 (Ser463/465) (Cell signaling) 1:50, anti-Yap1
786 (Lecaudey lab) 1:200. Secondary antibodies: goat anti-chicken Alexa Fluor 488 IgY (H+L) (In
787 vitrogen), goat anti-mouse IgG Cy3 conjugate (H+L) ((Life technologies) and goat anti-rabbit
788 Alexa Fluor 647 (ThermoFisher) were used at 1:500.
789 To test the effects of Verteporfin treatment, embryos were rinsed in fish tank water before being
790 fixed and processed as described above.
791 *avcPE cell quantification:*
792 We performed whole-mount immunofluorescent staining on control and mutant embryos in the
793 *epi:GFP* reporter line background and imaged the heart using a confocal microscope with a z-
794 step of 10 µm. The different tissues were labeled using anti-myosin heavy chain (MHC)
795 (myocardium) and anti-GFP (*epi:GFP*) antibodies, and DAPI dye to stain for nuclei. We then
796 manually quantified the number of avcPE cells per z slice. We identified the avcPE clusters
797 anatomically: avcPE clusters form in the dorsal pericardium, close to the atrio-ventricular canal
798 (avc). PE cells were identified by their rounded morphology in conjunction with their
799 expression of GFP (although some pericardial cells are also GFP-positive, they can be excluded
800 due to their flat morphology). In order to count each cell only once in the z-stack, we only
801 counted a cell when its nucleus was visible.
802 *Myocardial cell quantification:*
803 We performed whole-mount immunofluorescent staining on control and mutant embryos using
804 anti-myosin heavy chain (MHC) (myocardium) antibody and DAPI dye (nuclei). We imaged
805 the heart using a confocal microscope with a z-step of 10 µm. We then manually quantified the
806 number of myocardial cells per z slice (nuclei surrounded by MHC signal).
807 *In situ hybridization (ISH):*

808 ISH was performed in whole embryos according to (Thisse and Thisse, 2008) with minor
809 modifications. Antisense mRNA probe used was against full coding sequence of *bmp4*.
810 *In vivo imaging:*
811 ZF embryos were staged, anaesthetised with 0.02% tricaine solution and mounted in 0.7% low
812 melting-point agarose (Sigma Aldrich). Confocal imaging was performed on a Leica SP8
813 confocal microscope. Images were acquired bidirectionally with a low-magnification water
814 immersion objective (Leica HCX IRAPO L, 25X, N.A. 0.95). For time lapse, z-stacks were
815 acquired each 15 or 30 min, depending on the experiment. The optical plane was moved 15 µm
816 between z-sections.
817 Bright field experiments were performed on a Leica DMIRBE inverted microscope using a
818 Photron SA3 high speed CMOS camera (Photron, San Diego, CA) and water immersion
819 objective (Leica 20X, NA 0.7). Image sequences were acquired at a frame rate of 150 frames
820 per second.
821 *Mouse models:*
822 *Ift20*$^{null/+}$ (88) and *Ift88*$^{null/+}$ (89) mice were maintained on a C57BL/6JRj and B6D2 genetic
823 background respectively. Animal procedures were approved by the ethical committee of the
824 Institut Pasteur and the French Ministry of Research. E9.5 embryos were isolated in 200ng/ml
825 cold heparin, incubated in cold 250mM KCl and fixed in 4% paraformaldehyde in PBS inside
826 a rotative oven at 37°C overnight to remove excess of blood. Male and female samples were
827 mixed.
828 *Whole mount immunofluorescence in the mouse:*
829 Embryos were fixed in paraformaldehyde. The cardiac region was dissected, permeabilised in
830 0.75% Triton. Aldehydes were quenched with 2.6mg/ml NH4Cl. Immunostaining was
831 performed in 10% inactivated horse serum, 0,5% Triton with a primary antibody against Wt1

832 (Santa Cruz sc-192, 1:50), and with Alexa Fluor conjugated secondary antibodies (1:300) and
833 counterstained with Hoechst (1 :400). 80% glycerol was used to make the samples transparent.
834 *Mice PE volume analysis:*
835 Whole mount embryos stained with Wt1 antibody (Santa Cruz) were scanned on TCS SP8 DLS
836 (Digital Light Sheet) Leica with a water immersion objective (HC APO L, 10X, 0.3). Z-stacks
837 were taken every 2 µm. Both, coronal and sagittal views were acquired, if possible, for a more
838 precise analysis. **(Supp. 2 F)** Using Matlab software, the contour of the PE was manually drawn
839 (Wt1 signal) for each z plane and the area (A) was calculated. Volume (V) was estimated as:
840 $V = \Sigma zn\ Ai \times dz$; $i=1$; zn=number of planes; $dz= 2$ µm
841 3D images were reconstructed using IMARIS software (Bitplane Scientific Software).
842 *Immunofluorescence on cryosections in the mouse:*
843 Embryos were embedded in 7% gelatin, 15% sucrose, frozen in cold isopentane and sectioned
844 on a cryostat (10 µm). Immunostaining was performed on cryosections as described above, with
845 permeabilisation in 0.5% Triton, and with an additional incubation in 0.2 mg/mL goat anti-
846 mouse IgG Fab fragment to reduce non-specific reactivity of antibodies raised in the mouse.
847 Primary antibodies against Tbx18 (Santa Cruz sc-17869, 1:100), Wt1 (Santa Cruz sc-192, 1:50),
848 Yap1 (Santa Cruz sc-101199, 1:100), Amotl1 (Sigma HPA001196, 1:50) and p-Smad1/5/9
849 (Cell signaling 13820, 1:250) were used, with Alexa Fluor conjugated secondary antibodies
850 (1:500) and Hoechst nuclear counterstaining (1:1000). Samples were imaged in DAKO
851 mounting medium on a LSM700 (Zeiss) confocal microscope with a 40X/1.3 objective. Z-
852 stacks were taken every 0.9 µm.
853 *Yap1- and Amotl1-positive cell quantifications:*
854 Nuclei positions on the slides were defined using IMARIS (Bitplane Scientific Software) Spots
855 detection function. The results were manually corrected if needed. Nuclei positions were
856 exported from Imaris and imported to Matlab. Each cell was assigned a unique index. The

857 intensity of Tbx18 signal was evaluated in correspondence with the nuclei positions. Cells
858 where the intensity was found higher than a threshold were considered positive. The threshold
859 was established according to the background noise intensity. Results were manually corrected
860 if needed and Tbx18-positive cells were automatically counted. Yap1 signal was visualized in
861 fire LUT to facilitate perception of signal intensity. Nuclear Yap1-positive cells (higher signal
862 in the nucleus than in the cytoplasm) were manually defined through index identification of
863 cells and counted automatically. The same procedure was followed for Amotl1 signal. The
864 outline of the outer PE region was manually drawn and areas of the two regions were calculated
865 automatically. Matlab provided the total positive cell number for each signal and area, including
866 signal co-localization **(Supp. 3 E)**.

867 *Cell culture, siRNAs and transfection:*

868 Cells were cultured in appropriate conditions: MDCK (MEM Eagle - Earle's BSS, 10 % FCS,
869 AANE 0.1 mM, Sodium Pyruvate 1mM, Gentamicin 40 µg/ml), HeLa (DMEM 4.5 g/l glucose,
870 10% FCS, Penicillin 100 UI/ml, Streptomycin 100 µg/ml), HEK293 cells (DMEM 1g/L glucose,
871 FCS 10%, Penicillin 100 UI/ml, Streptomycin 100 µg/ml) and DLD-1 (DMEM 4.5 g/l glucose,
872 10% FCS, Penicillin 100 UI/ml, Streptomycin 100 µg/ml)siRNA (Dharmacon) ON-Target plus
873 - Control pool Non-targeting (D-001810-10-05) and SMART pool human IFT88 (L-012281-
874 01) were used at 50 nM working concentration. Cells were transfected 16h after splitting using
875 Opti-MEM medium and Oligofectamine reagent.

876 *Generation of DLD-1 IFT88-AID targeted cells:*

877 DLD-1 IFT88-AID cells were generated by adding an AID tag followed by a YFP tag at the 3′
878 end of the last exon on the IFT88 genomic locus. In detail, a clonal population of DLD-1 cells
879 stably expressing TIR1-9xMyc protein was used for targeting (90). sgRNA targeting two
880 regions adjacent to the 3′ end of IFT88 gene were introduced under the control of U6
881 transcription promoter into two separate vectors encoding for the expression of the Cas9 nickase

882 (D10A) (91) (addgene 42335). A donor construct containing ≈ 600 bp recombination arms
883 surrounding the 3′ end of IFT88 locus, in frame with a sequence encoding for an AID-YFP-
884 Stop sequence, was generated. All three vectors were transfected into DLD-1 TIR1 cells using
885 Xtreme Gene 9 DNA transfection reagent (Roche). Cells were sorted based on their YFP
886 fluorescence and single clones were isolated. Homozygous targeted clones were identified by
887 PCR. Targeting of IFT88 and degradation of IFT88-AID-YFP was confirmed by immunoblot
888 following addition of Auxin (Sigma-Aldrich) at 500 µM in the culture medium for the indicated
889 times.

890 *Immunofluorescence on cells:*

891 Cells were fixed in 100% MeOH for 6 min at -20°C (Ift88 and γ-tubulin antibodies), in 4% PFA
892 for 7 min at RT (DLD-1 cells. Yap1 antibody) or in PFA 4% for 17 min at RT (MDCK and
893 HeLa cells. Yap/Taz antibody). After washing in 0.1% PBS Tween20, cells were permeabilized
894 in 0.5% PBS-NP40 and blocked in 5% BSA 1h at RT. Primary antibodies were added in the
895 blocking solution and incubated overnight at 4°C. Secondary antibodies were added in 0.1%
896 PBS Tween20 after washing and incubated for 2h at RT. Then cells were incubated with DAPI
897 (Invitrogen), 1:1000, for 15 min at RT. After being thoroughly washed, samples were mounted
898 for imaging on a Leica SP5 (siRNA experiments) or SP8 (DLD-1 experiments and experiments
899 to assess subcellular localization) confocal microscope with an oil immersion objective (Leica
900 HCX PL APO lambda blue, 63X, N.A. 1.4). Z-stacks were taken every 1 µm.

901 Antibodies used were as follows: anti-γ-tubulin (Santa Cruz) 1:500, anti-α-tubulin (Sigma,
902 1:2000), anti-IFT88 (Euromedex) 1:50, anti-Yap1 (4912) (Cell signaling) 1:50 (DLD-1
903 experiments), and anti-Yap/Taz (D24E4) (Cell signaling) 1:50 (MDCK and HeLa siRNA
904 experiments). Secondary antibodies: goat anti-mouse IgG Cy3 conjugate (H+L) (Life
905 technologies) and goat anti-rabbit Alexa Fluor 647 (In vitrogen) were used at 1:500.

906 *Nuclear Yap quantifications:*

907 Analyses were performed using Image J. Nuclei areas were selected manually using DAPI
908 signal as reference on z-projection images (sum slices for DLD-1 experiment and maximum
909 intensity projection for siRNA experiments). Yap average nuclear signal intensity was
910 measured for the selected areas. In experiments in DLD-1 cells the values were measured for
911 each individual nucleus, while in the case of siRNA experiments, all the nuclei in a slice were
912 measured together. Values were normalized to their controls in order to merge data from
913 different experiments.

914 *Nuclear/cytoplasmic Yap1 ratio:*

915 Analyses were performed using Image J. Nuclei areas were selected manually using DAPI
916 signal as reference on z-projection images (sum slices). Cytoplasmic areas were selected using
917 α-tubulin signal as reference. Yap average nuclear signal intensity was measured for the nuclear
918 ROI. Yap average cytoplasmic signal intensity was measured after subtracting nuclear ROI
919 from the cytoplasmic ROI.

920 *Lysates and immunoblotting:*

921 DLD-1 cell extracts were obtained after lysis with Laemmli sample buffer of an equal number
922 of cells for each sample. Proteins were resolved by SDS-PAGE, transferred to nitrocellulose
923 membranes and revealed by immunoblot using Western Lightning Plus-ECL kit (PerkinElmer).

924 *Immunoprecipitation (IP) assays:*

925 HEK293 cells:

926 HEK293 cells (Q-BIOgene AES0503) were co-transfected with plasmids Flag-Amotl1 (92) and
927 Ift20-GFP (9), or a Flag-control plasmid using Lipofectamine® 2000 Transfection Reagent
928 (ThermoFisher SCIENTIFIC) and cultured for 48h. Proteins were extracted in a lysis buffer
929 (10mMTris-Cl pH 7.5, 5mM EDTA, 150mM NaCl, 10% glycerol and 5% CHAPS) in the
930 presence of protease inhibitors (cOmpleteTM Protease Inhibitor Cocktail, Roche).
931 Immunoprecipitation of protein extracts was performed using a monoclonal anti-Flag antibody

932 covalently attached to agarose (Anti-FLAG M2 Affinity gel, Sigma). Proteins were eluted in
933 2xNuPAGE LDS Sample Buffer (ThermoFisher). Proteins were separated on SDS–
934 polyacrylamide gel electrophoresis and transferred to a nitrocellulose membrane. Proteins were
935 detected with the primary antibodies against Flag (1:1000, Sigma F7425), GFP (1:1000,
936 ThermoFisher CAB421), Ift20 (1:500, Proteintech, 13615-1-AP), Yap1 (1:1000, Cell Signaling
937 4912S) and Amotl1 (1:1000, Sigma HPA001196), followed by HRP-conjugated secondary
938 antibodies (1:5000, Jackson ImmunoResearch) and the ECL detection reagent.
939 HeLa cells:
940 We performed IPs using GFP-Trap (ChromoTek) agarose beads in two conditions: Control IP
941 (YAP1-Myc (93), pEGFP-C1 and HA-Amotl1(23)) and IFT88 IP (YAP1-Myc, IFT88-GFP (94)
942 and HA-Amotl1). HeLa cells (2x 10cm dish/ condition) were transfected with Lipofectamine
943 2000. Experiments were performed using the following setup: Cells were seeded at high density
944 into 10cm dishes and transfected 16 hrs after seeding at 95% confluency. Twenty-four hours
945 post-transfection, cells were seeded into 15cm dishes in order to achieve culture of isolated cells
946 (10x 15cm dish/ condition). Proteins were extracted 60 hrs post-transfection in a lysis buffer
947 (10mM TrisHCl, pH7.5; 150mM NaCl; 0.5mM EDTA; 0.5% NP-40; protease inhibitors
948 Complete). GFP beads were washed once in lysis buffer and incubated with 16 mg of the protein
949 lysate for 16 hrs at 4 ^{0}C. Beads were washed four times in buffer without detergent and proteins
950 were eluted by boiling for 10 mins. The input (1%) and IP were analyzed using immunoblot
951 and the membranes were probed with anti-GFP (Abcam), anti-Yap/TAZ (D24E4, Cell
952 Signaling) and anti-HA (Sigma Aldrich) antibodies.
953 Statistics:
954 We applied D'Agostino & Pearson and Shapiro-Wilk normality tests to assess whether the
955 samples fit a normal distribution and F test to compare variances. For normal distributed and
956 homoscedastic samples, we used t-test or ANOVA. For non-parametric samples, we applied

957 Man-Whitney or Kruskal-Wallis. The pertinent statistical analyses for each experiment were
958 performed using GraphPad Prism 7 software. For the analysis of nuclear p-smad 1/5/9 and
959 YAP1 signal in mice we used the non-parametric Chi-squared test of homogeneity to test
960 whether the observed frequency of positive nuclei was equally distributed across the *wild type*
961 and mutant embryos.
962
963
964
965
966

967 1. Berbari NF, O'Connor AK, Haycraft CJ, Yoder BK. The Primary Cilium as a Complex
968 Signaling Center. Curr Biol [Internet]. 2009 Jul 14 [cited 2018 Sep 6];19(13):R526–35.
969 Available from: http://www.ncbi.nlm.nih.gov/pubmed/19602418
970 2. Reiter JF, Leroux MR. Genes and molecular pathways underpinning ciliopathies. Nat
971 Rev Mol Cell Biol [Internet]. 2017 Jul 12 [cited 2018 Sep 6];18(9):533–47. Available
972 from: http://www.ncbi.nlm.nih.gov/pubmed/28698599
973 3. Slough J, Cooney L, Brueckner M. Monocilia in the embryonic mouse heart suggest a
974 direct role for cilia in cardiac morphogenesis. Dev Dyn [Internet]. 2008 Sep [cited 2018
975 Sep 6];237(9):2304–14. Available from:
976 http://www.ncbi.nlm.nih.gov/pubmed/18729223
977 4. Li Y, Klena NT, Gabriel GC, Liu X, Kim AJ, Lemke K, et al. Global genetic analysis
978 in mice unveils central role for cilia in congenital heart disease. Nature [Internet]. 2015
979 May 25 [cited 2018 Sep 6];521(7553):520–4. Available from:
980 http://www.ncbi.nlm.nih.gov/pubmed/25807483
981 5. San Agustin JT, Klena N, Granath K, Panigrahy A, Stewart E, Devine W, et al. Genetic

982 link between renal birth defects and congenital heart disease. Nat Commun [Internet].
983 2016 Mar 22 [cited 2018 Sep 6];7:11103. Available from:
984 http://www.ncbi.nlm.nih.gov/pubmed/27002738
985 6. Klena N, Gabriel G, Liu X, Yagi H, Li Y, Chen Y, et al. Role of Cilia and Left-Right
986 Patterning in Congenital Heart Disease [Internet]. Etiology and Morphogenesis of
987 Congenital Heart Disease: From Gene Function and Cellular Interaction to
988 Morphology. 2016 [cited 2018 Sep 6]. Available from:
989 http://www.ncbi.nlm.nih.gov/pubmed/29787118
990 7. Rosenbaum JL, Witman GB. Intraflagellar transport. Nat Rev Mol Cell Biol [Internet].
991 2002 Nov 1 [cited 2018 Sep 6];3(11):813–25. Available from:
992 http://www.ncbi.nlm.nih.gov/pubmed/12415299
993 8. Taschner M, Bhogaraju S, Lorentzen E. Architecture and function of IFT complex
994 proteins in ciliogenesis. Differentiation [Internet]. 2012 Feb [cited 2018 Sep
995 6];83(2):S12–22. Available from: http://www.ncbi.nlm.nih.gov/pubmed/22118932
996 9. Follit JA, Tuft RA, Fogarty KE, Pazour GJ. The Intraflagellar Transport Protein IFT20
997 Is Associated with the Golgi Complex and Is Required for Cilia Assembly. Margolis B,
998 editor. Mol Biol Cell [Internet]. 2006 Sep [cited 2018 Sep 6];17(9):3781–92. Available
999 from: http://www.ncbi.nlm.nih.gov/pubmed/16775004
1000 10. Omori Y, Zhao C, Saras A, Mukhopadhyay S, Kim W, Furukawa T, et al. elipsa is an
1001 early determinant of ciliogenesis that links the IFT particle to membrane-associated
1002 small GTPase Rab8. Nat Cell Biol [Internet]. 2008 Apr 23 [cited 2018 Sep
1003 6];10(4):437–44. Available from: http://www.ncbi.nlm.nih.gov/pubmed/18364699
1004 11. Zhu X, Liang Y, Gao F, Pan J. IFT54 regulates IFT20 stability but is not essential for
1005 tubulin transport during ciliogenesis. Cell Mol Life Sci [Internet]. 2017 Sep 17 [cited
1006 2018 Sep 6];74(18):3425–37. Available from:

1007 http://www.ncbi.nlm.nih.gov/pubmed/28417161
1008 12. Pazour GJ, Dickert BL, Vucica Y, Seeley ES, Rosenbaum JL, Witman GB, et al.
1009 Chlamydomonas IFT88 and its mouse homologue, polycystic kidney disease gene
1010 tg737, are required for assembly of cilia and flagella. J Cell Biol [Internet]. 2000 Oct
1011 30 [cited 2018 Sep 6];151(3):709–18. Available from:
1012 http://www.ncbi.nlm.nih.gov/pubmed/11062270
1013 13. Hua K, Ferland RJ. Primary cilia proteins: ciliary and extraciliary sites and functions.
1014 Cell Mol Life Sci [Internet]. 2018 May [cited 2018 Sep 6];75(9):1521–40. Available
1015 from: http://www.ncbi.nlm.nih.gov/pubmed/29305615
1016 14. Vertii A, Bright A, Delaval B, Hehnly H, Doxsey S. New frontiers: discovering cilia-
1017 independent functions of cilia proteins. EMBO Rep [Internet]. 2015 Oct 1 [cited 2018
1018 Sep 6];16(10):1275–87. Available from:
1019 http://www.ncbi.nlm.nih.gov/pubmed/26358956
1020 15. Delaval B, Bright A, Lawson ND, Doxsey S. The cilia protein IFT88 is required for
1021 spindle orientation in mitosis. Nat Cell Biol [Internet]. 2011 Apr 27 [cited 2018 Sep
1022 6];13(4):461–8. Available from: http://www.ncbi.nlm.nih.gov/pubmed/21441926
1023 16. Taulet N, Vitre B, Anguille C, Douanier A, Rocancourt M, Taschner M, et al. IFT
1024 proteins spatially control the geometry of cleavage furrow ingression and lumen
1025 positioning. Nat Commun [Internet]. 2017 Dec 4 [cited 2018 Sep 13];8(1):1928.
1026 Available from: http://www.nature.com/articles/s41467-017-01479-3
1027 17. Robert A, Margall-Ducos G, Guidotti J-E, Bregerie O, Celati C, Brechot C, et al. The
1028 intraflagellar transport component IFT88/polaris is a centrosomal protein regulating
1029 G1-S transition in non-ciliated cells. J Cell Sci [Internet]. 2007 Feb 15 [cited 2018 Sep
1030 6];120(4):628–37. Available from: http://www.ncbi.nlm.nih.gov/pubmed/17264151
1031 18. Finetti F, Paccani SR, Riparbelli MG, Giacomello E, Perinetti G, Pazour GJ, et al.

1032 Intraflagellar transport is required for polarized recycling of the TCR/CD3 complex to
1033 the immune synapse. Nat Cell Biol [Internet]. 2009 Nov 25 [cited 2018 Sep
1034 6];11(11):1332–9. Available from: http://www.ncbi.nlm.nih.gov/pubmed/19855387
1035 19. Galgano D, Onnis A, Pappalardo E, Galvagni F, Acuto O, Baldari CT. The T cell
1036 IFT20 interactome reveals new players in immune synapse assembly. J Cell Sci
1037 [Internet]. 2017 Feb 2 [cited 2018 Sep 6];130(6):jcs.200006. Available from:
1038 http://www.ncbi.nlm.nih.gov/pubmed/28154159
1039 20. Xin M, Kim Y, Sutherland LB, Qi X, McAnally J, Schwartz RJ, et al. Regulation of
1040 Insulin-Like Growth Factor Signaling by Yap Governs Cardiomyocyte Proliferation
1041 and Embryonic Heart Size. Sci Signal [Internet]. 2011 Oct 25 [cited 2018 Sep
1042 17];4(196):ra70–ra70. Available from: http://www.ncbi.nlm.nih.gov/pubmed/22028467
1043 21. Fukui H, Miyazaki T, Chow RW-Y, Ishikawa H, Nakajima H, Vermot J, et al. Hippo
1044 signaling determines the number of venous pole cells that originate from the anterior
1045 lateral plate mesoderm in zebrafish. Elife [Internet]. 2018 May 29 [cited 2018 Sep 6];7.
1046 Available from: https://elifesciences.org/articles/29106
1047 22. Lai JKH, Collins MM, Uribe V, Jiménez-Amilburu V, Günther S, Maischein H-M, et
1048 al. The Hippo pathway effector Wwtr1 regulates cardiac wall maturation in zebrafish.
1049 Development [Internet]. 2018 May 15 [cited 2018 Sep 6];145(10):dev159210.
1050 Available from: http://www.ncbi.nlm.nih.gov/pubmed/29773645
1051 23. Ragni C V., Diguet N, Le Garrec J-F, Novotova M, Resende TP, Pop S, et al. Amotl1
1052 mediates sequestration of the Hippo effector Yap1 downstream of Fat4 to restrict heart
1053 growth. Nat Commun [Internet]. 2017 Feb 27 [cited 2018 Sep 6];8:14582. Available
1054 from: http://www.ncbi.nlm.nih.gov/pubmed/28239148
1055 24. Leach JP, Heallen T, Zhang M, Rahmani M, Morikawa Y, Hill MC, et al. Hippo
1056 pathway deficiency reverses systolic heart failure after infarction. Nature [Internet].

1057 2017 Oct 4 [cited 2018 Sep 6];550(7675):260–4. Available from:
1058 http://www.ncbi.nlm.nih.gov/pubmed/28976966
1059 25. Bassat E, Mutlak YE, Genzelinakh A, Shadrin IY, Baruch Umansky K, Yifa O, et al.
1060 The extracellular matrix protein agrin promotes heart regeneration in mice. Nature
1061 [Internet]. 2017 Jun 13 [cited 2018 Sep 6];547(7662):179–84. Available from:
1062 http://www.nature.com/doifinder/10.1038/nature22978
1063 26. Singh A, Ramesh S, Cibi DM, Yun LS, Li J, Li L, et al. Hippo Signaling Mediators
1064 Yap and Taz Are Required in the Epicardium for Coronary Vasculature Development.
1065 Cell Rep [Internet]. 2016 May 17 [cited 2018 Sep 6];15(7):1384–93. Available from:
1066 http://www.ncbi.nlm.nih.gov/pubmed/27160901
1067 27. Elosegui-Artola A, Andreu I, Beedle AEM, Lezamiz A, Uroz M, Kosmalska AJ, et al.
1068 Force Triggers YAP Nuclear Entry by Regulating Transport across Nuclear Pores. Cell
1069 [Internet]. 2017 Nov 30 [cited 2018 Sep 6];171(6):1397-1410.e14. Available from:
1070 http://www.ncbi.nlm.nih.gov/pubmed/29107331
1071 28. Bratt A, Wilson WJ, Troyanovsky B, Aase K, Kessler R, Van Meir EG, et al.
1072 Angiomotin belongs to a novel protein family with conserved coiled-coil and PDZ
1073 binding domains. Gene [Internet]. 2002 Sep 18 [cited 2018 Sep 6];298(1):69–77.
1074 Available from: http://www.ncbi.nlm.nih.gov/pubmed/12406577
1075 29. Zheng Y, Vertuani S, Nyström S, Audebert S, Meijer I, Tegnebratt T, et al.
1076 Angiomotin-like protein 1 controls endothelial polarity and junction stability during
1077 sprouting angiogenesis. Circ Res [Internet]. 2009 Jul 31 [cited 2018 Sep
1078 6];105(3):260–70. Available from:
1079 http://circres.ahajournals.org/cgi/doi/10.1161/CIRCRESAHA.109.195156
1080 30. DeRan M, Yang J, Shen C-H, Peters EC, Fitamant J, Chan P, et al. Energy Stress
1081 Regulates Hippo-YAP Signaling Involving AMPK-Mediated Regulation of

1082 Angiomotin-like 1 Protein. Cell Rep [Internet]. 2014 Oct 23 [cited 2018 Sep
1083 6];9(2):495–503. Available from: http://www.ncbi.nlm.nih.gov/pubmed/25373897
1084 31. Zhao B, Li L, Lu Q, Wang LH, Liu C-Y, Lei Q, et al. Angiomotin is a novel Hippo
1085 pathway component that inhibits YAP oncoprotein. Genes Dev [Internet]. 2011 Jan 1
1086 [cited 2018 Sep 6];25(1):51–63. Available from:
1087 http://www.ncbi.nlm.nih.gov/pubmed/21205866
1088 32. Wang W, Huang J, Chen J. Angiomotin-like Proteins Associate with and Negatively
1089 Regulate YAP1. J Biol Chem [Internet]. 2011 Feb 11 [cited 2018 Sep 6];286(6):4364–
1090 70. Available from: http://www.ncbi.nlm.nih.gov/pubmed/21187284
1091 33. Agarwala S, Duquesne S, Liu K, Boehm A, Grimm L, Link S, et al. Amotl2a interacts
1092 with the Hippo effector Yap1 and the Wnt/β-catenin effector Lef1 to control tissue size
1093 in zebrafish. Elife [Internet]. 2015 Sep 3 [cited 2018 Sep 6];4:e08201. Available from:
1094 http://www.ncbi.nlm.nih.gov/pubmed/26335201
1095 34. Nakajima H, Yamamoto K, Agarwala S, Terai K, Fukui H, Fukuhara S, et al. Flow-
1096 Dependent Endothelial YAP Regulation Contributes to Vessel Maintenance. Dev Cell
1097 [Internet]. 2017 Mar 27 [cited 2018 Sep 6];40(6):523-536.e6. Available from:
1098 http://www.ncbi.nlm.nih.gov/pubmed/28350986
1099 35. Habbig S, Bartram MP, Sägmüller JG, Griessmann A, Franke M, Müller R-U, et al.
1100 The ciliopathy disease protein NPHP9 promotes nuclear delivery and activation of the
1101 oncogenic transcriptional regulator TAZ. Hum Mol Genet [Internet]. 2012 Dec 15
1102 [cited 2018 Sep 6];21(26):5528–38. Available from:
1103 http://www.ncbi.nlm.nih.gov/pubmed/23026745
1104 36. Frank V, Habbig S, Bartram MP, Eisenberger T, Veenstra-Knol HE, Decker C, et al.
1105 Mutations in NEK8 link multiple organ dysplasia with altered Hippo signalling and
1106 increased c-MYC expression. Hum Mol Genet [Internet]. 2013 Jun 1 [cited 2018 Sep

1107 6];22(11):2177–85. Available from: http://www.ncbi.nlm.nih.gov/pubmed/23418306
1108 37. Grampa V, Delous M, Zaidan M, Odye G, Thomas S, Elkhartoufi N, et al. Novel
1109 NEK8 Mutations Cause Severe Syndromic Renal Cystic Dysplasia through YAP
1110 Dysregulation. Beier DR, editor. PLOS Genet [Internet]. 2016 Mar 11 [cited 2018 Sep
1111 6];12(3):e1005894. Available from: http://www.ncbi.nlm.nih.gov/pubmed/26967905
1112 38. Kim M, Kim M, Lee M-S, Kim C-H, Lim D-S. The MST1/2-SAV1 complex of the
1113 Hippo pathway promotes ciliogenesis. Nat Commun [Internet]. 2014 Dec 4 [cited 2018
1114 Sep 6];5(1):5370. Available from: http://www.ncbi.nlm.nih.gov/pubmed/25367221
1115 39. Männer J, Schlueter J, Brand T. Experimental analyses of the function of the
1116 proepicardium using a new microsurgical procedure to induce loss-of-proepicardial-
1117 function in chick embryos. Dev Dyn [Internet]. 2005 Aug [cited 2018 Sep
1118 6];233(4):1454–63. Available from: http://www.ncbi.nlm.nih.gov/pubmed/15977171
1119 40. Moore AW, McInnes L, Kreidberg J, Hastie ND, Schedl A. YAC complementation
1120 shows a requirement for Wt1 in the development of epicardium, adrenal gland and
1121 throughout nephrogenesis. Development [Internet]. 1999 May [cited 2018 Sep
1122 6];126(9):1845–57. Available from: http://www.ncbi.nlm.nih.gov/pubmed/10101119
1123 41. Wu S-P, Dong X-R, Regan JN, Su C, Majesky MW. Tbx18 regulates development of
1124 the epicardium and coronary vessels. Dev Biol [Internet]. 2013 Nov 15 [cited 2018 Sep
1125 6];383(2):307–20. Available from: http://www.ncbi.nlm.nih.gov/pubmed/24016759
1126 42. González-Rosa JM, Peralta M, Mercader N. Pan-epicardial lineage tracing reveals that
1127 epicardium derived cells give rise to myofibroblasts and perivascular cells during
1128 zebrafish heart regeneration. Dev Biol [Internet]. 2012 Oct 15 [cited 2018 Sep
1129 6];370(2):173–86. Available from: http://www.ncbi.nlm.nih.gov/pubmed/22877945
1130 43. Kikuchi K, Poss KD. Cardiac Regenerative Capacity and Mechanisms. Annu Rev Cell
1131 Dev Biol [Internet]. 2012 Nov 10 [cited 2018 Sep 6];28(1):719–41. Available from:

1132 http://www.ncbi.nlm.nih.gov/pubmed/23057748
1133 44. Limana F, Capogrossi MC, Germani A. The epicardium in cardiac repair: From the
1134 stem cell view. Pharmacol Ther [Internet]. 2011 Jan [cited 2018 Sep 6];129(1):82–96.
1135 Available from: http://www.ncbi.nlm.nih.gov/pubmed/20937304
1136 45. Katz TC, Singh MK, Degenhardt K, Rivera-Feliciano J, Johnson RL, Epstein JA, et al.
1137 Distinct Compartments of the Proepicardial Organ Give Rise to Coronary Vascular
1138 Endothelial Cells. Dev Cell [Internet]. 2012 Mar 13 [cited 2018 Sep 6];22(3):639–50.
1139 Available from: http://www.ncbi.nlm.nih.gov/pubmed/22421048
1140 46. Peralta M, Steed E, Harlepp S, González-Rosa JM, Monduc F, Ariza-Cosano A, et al.
1141 Heartbeat-driven pericardiac fluid forces contribute to epicardium morphogenesis. Curr
1142 Biol [Internet]. 2013 Sep 23 [cited 2018 Sep 6];23(18):1726–35. Available from:
1143 http://linkinghub.elsevier.com/retrieve/pii/S0960982213008282
1144 47. Mikawa T, Fischman DA. Retroviral analysis of cardiac morphogenesis: discontinuous
1145 formation of coronary vessels. Proc Natl Acad Sci U S A [Internet]. 1992 Oct 15 [cited
1146 2018 Sep 6];89(20):9504–8. Available from:
1147 http://www.ncbi.nlm.nih.gov/pubmed/1409660
1148 48. Mikawa T, Gourdie RG. Pericardial Mesoderm Generates a Population of Coronary
1149 Smooth Muscle Cells Migrating into the Heart along with Ingrowth of the Epicardial
1150 Organ. Dev Biol [Internet]. 1996 Mar 15 [cited 2018 Sep 6];174(2):221–32. Available
1151 from: http://www.ncbi.nlm.nih.gov/pubmed/8631495
1152 49. Acharya A, Baek ST, Huang G, Eskiocak B, Goetsch S, Sung CY, et al. The bHLH
1153 transcription factor Tcf21 is required for lineage-specific EMT of cardiac fibroblast
1154 progenitors. Development [Internet]. 2012 Jun 15 [cited 2018 Sep 6];139(12):2139–49.
1155 Available from: http://dev.biologists.org/cgi/doi/10.1242/dev.079970
1156 50. Liu J, Stainier DYR. Tbx5 and Bmp Signaling Are Essential for Proepicardium

1157 Specification in Zebrafish. Circ Res [Internet]. 2010 Jun 25 [cited 2018 Sep
1158 6];106(12):1818–28. Available from: http://www.ncbi.nlm.nih.gov/pubmed/20413782
1159 51. Ishii Y, Garriock RJ, Navetta AM, Coughlin LE, Mikawa T. BMP Signals Promote
1160 Proepicardial Protrusion Necessary for Recruitment of Coronary Vessel and Epicardial
1161 Progenitors to the Heart. Dev Cell [Internet]. 2010 Aug [cited 2018 Sep 6];19(2):307–
1162 16. Available from: http://linkinghub.elsevier.com/retrieve/pii/S153458071000345X
1163 52. Schlueter J, Männer J, Brand T. BMP is an important regulator of proepicardial identity
1164 in the chick embryo. Dev Biol [Internet]. 2006 Jul 15 [cited 2018 Sep 6];295(2):546–
1165 58. Available from: http://linkinghub.elsevier.com/retrieve/pii/S0012160606002405
1166 53. Tsujikawa M, Malicki J. Intraflagellar transport genes are essential for differentiation
1167 and survival of vertebrate sensory neurons. Neuron [Internet]. 2004 Jun 10 [cited 2018
1168 Sep 6];42(5):703–16. Available from: http://www.ncbi.nlm.nih.gov/pubmed/15182712
1169 54. Tay SY, Yu X, Wong KN, Panse P, Ng CP, Roy S. The iguana/DZIP1 protein is a
1170 novel component of the ciliogenic pathway essential for axonemal biogenesis. Dev
1171 Dyn [Internet]. 2010 Feb [cited 2018 Sep 6];239(2):527–34. Available from:
1172 http://www.ncbi.nlm.nih.gov/pubmed/20014402
1173 55. Kim H, Richardson J, van Eeden F, Ingham PW. Gli2a protein localization reveals a
1174 role for Iguana/DZIP1 in primary ciliogenesis and a dependence of Hedgehog signal
1175 transduction on primary cilia in the zebrafish. BMC Biol [Internet]. 2010 Apr 19 [cited
1176 2018 Sep 6];8(1):65. Available from:
1177 http://bmcbiol.biomedcentral.com/articles/10.1186/1741-7007-8-65
1178 56. Borovina A, Superina S, Voskas D, Ciruna B. Vangl2 directs the posterior tilting and
1179 asymmetric localization of motile primary cilia. Nat Cell Biol [Internet]. 2010 Apr 21
1180 [cited 2018 Sep 6];12(4):407–12. Available from:
1181 http://www.ncbi.nlm.nih.gov/pubmed/20305649

1182 57. Sun Z, Amsterdam A, Pazour GJ, Cole DG, Miller MS, Hopkins N. A genetic screen in
1183 zebrafish identifies cilia genes as a principal cause of cystic kidney. Development
1184 [Internet]. 2004 Aug 15 [cited 2019 Jul 15];131(16):4085–93. Available from:
1185 http://www.ncbi.nlm.nih.gov/pubmed/10804177
1186 58. Huang P, Schier AF. Dampened Hedgehog signaling but normal Wnt signaling in
1187 zebrafish without cilia. Development [Internet]. 2009 Sep 15 [cited 2018 Sep
1188 6];136(18):3089–98. Available from: http://www.ncbi.nlm.nih.gov/pubmed/19700616
1189 59. Carmona R, González-Iriarte M, Pérez-Pomares JM, Muñoz-Chápuli R. Localization of
1190 the Wilm's tumour protein WT1 in avian embryos. Cell Tissue Res [Internet]. 2001
1191 Feb [cited 2018 Sep 6];303(2):173–86. Available from:
1192 http://www.ncbi.nlm.nih.gov/pubmed/11291764
1193 60. Hansen CG, Moroishi T, Guan K-L. YAP and TAZ: a nexus for Hippo signaling and
1194 beyond. Trends Cell Biol [Internet]. 2015 Sep [cited 2018 Sep 17];25(9):499–513.
1195 Available from: http://www.ncbi.nlm.nih.gov/pubmed/26045258
1196 61. Miesfeld JB, Link BA. Establishment of transgenic lines to monitor and manipulate
1197 Yap/Taz-Tead activity in zebrafish reveals both evolutionarily conserved and divergent
1198 functions of the Hippo pathway. Mech Dev [Internet]. 2014 Aug [cited 2018 Sep
1199 6];133:177–88. Available from: http://www.ncbi.nlm.nih.gov/pubmed/24560909
1200 62. Liu-Chittenden Y, Huang B, Shim JS, Chen Q, Lee S-J, Anders RA, et al. Genetic and
1201 pharmacological disruption of the TEAD-YAP complex suppresses the oncogenic
1202 activity of YAP. Genes Dev [Internet]. 2012 Jun 15 [cited 2019 Jul 15];26(12):1300–5.
1203 Available from: http://www.ncbi.nlm.nih.gov/pubmed/22677547
1204 63. Wang W, Li N, Li X, Tran MK, Han X, Chen J. Tankyrase Inhibitors Target YAP by
1205 Stabilizing Angiomotin Family Proteins. Cell Rep [Internet]. 2015 Oct 20 [cited 2019
1206 Jul 15];13(3):524–32. Available from: http://www.ncbi.nlm.nih.gov/pubmed/26456820

1207 64. Lancaster MA, Schroth J, Gleeson JG. Subcellular spatial regulation of canonical Wnt
1208 signalling at the primary cilium. Nat Cell Biol [Internet]. 2011 Jun 22 [cited 2018 Sep
1209 13];13(6):700–7. Available from: http://www.ncbi.nlm.nih.gov/pubmed/21602792
1210 65. Cao Y, Park A, Sun Z. Intraflagellar transport proteins are essential for cilia formation
1211 and for planar cell polarity. J Am Soc Nephrol [Internet]. 2010 Aug 1 [cited 2018 Sep
1212 6];21(8):1326–33. Available from:
1213 http://www.jasn.org/cgi/doi/10.1681/ASN.2009091001
1214 66. Ocbina PJR, Eggenschwiler JT, Moskowitz I, Anderson K V. Complex interactions
1215 between genes controlling trafficking in primary cilia. Nat Genet [Internet]. 2011 Jun 8
1216 [cited 2019 Jul 30];43(6):547–53. Available from:
1217 http://www.ncbi.nlm.nih.gov/pubmed/21552265
1218 67. Zanconato F, Cordenonsi M, Piccolo S. YAP/TAZ at the Roots of Cancer. Cancer Cell
1219 [Internet]. 2016 Jun 13 [cited 2018 Sep 6];29(6):783–803. Available from:
1220 http://www.ncbi.nlm.nih.gov/pubmed/27300434
1221 68. Oh S-H, Swiderska-Syn M, Jewell ML, Premont RT, Diehl AM. Liver regeneration
1222 requires Yap1-TGFβ-dependent epithelial-mesenchymal transition in hepatocytes. J
1223 Hepatol [Internet]. 2018 Aug [cited 2018 Sep 6];69(2):359–67. Available from:
1224 http://www.ncbi.nlm.nih.gov/pubmed/29758331
1225 69. Artap S, Manderfield LJ, Smith CL, Poleshko A, Aghajanian H, See K, et al.
1226 Endocardial Hippo signaling regulates myocardial growth and cardiogenesis. Dev Biol
1227 [Internet]. 2018 Aug 1 [cited 2018 Sep 6];440(1):22–30. Available from:
1228 http://www.ncbi.nlm.nih.gov/pubmed/29727635
1229 70. Yu F-X, Zhao B, Guan K-L. Hippo Pathway in Organ Size Control, Tissue
1230 Homeostasis, and Cancer. Cell [Internet]. 2015 Nov 5 [cited 2018 Sep 6];163(4):811–
1231 28. Available from: http://www.ncbi.nlm.nih.gov/pubmed/26544935

1232 71. Thompson BJ, Sahai E. MST kinases in development and disease. J Cell Biol
1233 [Internet]. 2015 Sep 14 [cited 2018 Sep 6];210(6):871–82. Available from:
1234 http://www.ncbi.nlm.nih.gov/pubmed/26370497
1235 72. Sun Y, Yong KMA, Villa-Diaz LG, Zhang X, Chen W, Philson R, et al. Hippo/YAP-
1236 mediated rigidity-dependent motor neuron differentiation of human pluripotent
1237 stem cells. Nat Mater [Internet]. 2014 Jun 13 [cited 2018 Sep 6];13(6):599–604.
1238 Available from: http://www.ncbi.nlm.nih.gov/pubmed/24728461
1239 73. Yi C, Shen Z, Stemmer-Rachamimov A, Dawany N, Troutman S, Showe LC, et al. The
1240 p130 Isoform of Angiomotin Is Required for Yap-Mediated Hepatic Epithelial Cell
1241 Proliferation and Tumorigenesis. Sci Signal [Internet]. 2013 Sep 3 [cited 2018 Sep
1242 6];6(291):ra77–ra77. Available from: http://www.ncbi.nlm.nih.gov/pubmed/24003254
1243 74. Piccolo S, Dupont S, Cordenonsi M. The Biology of YAP/TAZ: Hippo Signaling and
1244 Beyond. Physiol Rev [Internet]. 2014 Oct [cited 2019 Jul 30];94(4):1287–312.
1245 Available from: http://www.ncbi.nlm.nih.gov/pubmed/25287865
1246 75. Vuong LT, Iomini C, Balmer S, Esposito D, Aaronson SA, Mlodzik M. Kinesin-2 and
1247 IFT-A act as a complex promoting nuclear localization of β-catenin during Wnt
1248 signalling. Nat Commun [Internet]. 2018 Dec 13 [cited 2019 Jul 18];9(1):5304.
1249 Available from: http://www.nature.com/articles/s41467-018-07605-z
1250 76. Behal RH, Miller MS, Qin H, Lucker BF, Jones A, Cole DG. Subunit Interactions and
1251 Organization of the *Chlamydomonas reinhardtii* Intraflagellar Transport Complex A
1252 Proteins. J Biol Chem [Internet]. 2012 Apr 6 [cited 2019 Jul 30];287(15):11689–703.
1253 Available from: http://www.ncbi.nlm.nih.gov/pubmed/22170070
1254 77. Piperno G, Siuda E, Henderson S, Segil M, Vaananen H, Sassaroli M. Distinct mutants
1255 of retrograde intraflagellar transport (IFT) share similar morphological and molecular
1256 defects. J Cell Biol [Internet]. 1998 Dec 14 [cited 2019 Jul 30];143(6):1591–601.

1257 Available from: http://www.ncbi.nlm.nih.gov/pubmed/9852153
1258 78. Iomini C, Li L, Esparza JM, Dutcher SK. Retrograde Intraflagellar Transport Mutants
1259 Identify Complex A Proteins With Multiple Genetic Interactions in *Chlamydomonas*
1260 *reinhardtii*. Genetics [Internet]. 2009 Nov [cited 2019 Jul 30];183(3):885–96.
1261 Available from: http://www.ncbi.nlm.nih.gov/pubmed/19720863
1262 79. Rudat C, Norden J, Taketo MM, Kispert A. Epicardial function of canonical Wnt-,
1263 Hedgehog-, Fgfr1/2-, and Pdgfra-signalling. Cardiovasc Res [Internet]. 2013 Dec 1
1264 [cited 2019 Jul 18];100(3):411–21. Available from:
1265 https://academic.oup.com/cardiovascres/article-lookup/doi/10.1093/cvr/cvt210
1266 80. Sugimoto K, Hui SP, Sheng DZ, Kikuchi K. Dissection of zebrafish shha function
1267 using site-specific targeting with a Cre-dependent genetic switch. Elife [Internet]. 2017
1268 May 17 [cited 2019 Jul 18];6. Available from:
1269 http://www.ncbi.nlm.nih.gov/pubmed/28513431
1270 81. Robb L, Mifsud L, Hartley L, Biben C, Copeland NG, Gilbert DJ, et al. epicardin: A
1271 novel basic helix-loop-helix transcription factor gene expressed in epicardium,
1272 branchial arch myoblasts, and mesenchyme of developing lung, gut, kidney, and
1273 gonads. Dev Dyn [Internet]. 1998 Sep [cited 2019 Jul 18];213(1):105–13. Available
1274 from: http://doi.wiley.com/10.1002/%28SICI%291097-
1275 0177%28199809%29213%3A1%3C105%3A%3AAID-AJA10%3E3.0.CO%3B2-1
1276 82. Andrés-Delgado L, Ernst A, Galardi-Castilla M, Bazaga D, Peralta M, Münch J, et al.
1277 Actin dynamics and the Bmp pathway drive apical extrusion of proepicardial cells.
1278 Development [Internet]. 2019 Jul 1 [cited 2019 Jul 18];146(13):dev174961. Available
1279 from: http://www.ncbi.nlm.nih.gov/pubmed/31175121
1280 83. Villalobos E, Criollo A, Schiattarella GG, Altamirano F, French KM, May HI, et al.
1281 Fibroblast Primary Cilia Are Required for Cardiac Fibrosis. Circulation [Internet].

1282 2019 May 14 [cited 2019 Jul 30];139(20):2342–57. Available from:
1283 https://www.ahajournals.org/doi/10.1161/CIRCULATIONAHA.117.028752
1284 84. Mönnich M, Borgeskov L, Breslin L, Jakobsen L, Rogowski M, Doganli C, et al.
1285 CEP128 Localizes to the Subdistal Appendages of the Mother Centriole and Regulates
1286 TGF-β/BMP Signaling at the Primary Cilium. Cell Rep [Internet]. 2018 Mar [cited
1287 2019 Jul 30];22(10):2584–92. Available from:
1288 https://linkinghub.elsevier.com/retrieve/pii/S2211124718302249
1289 85. Vion A-C, Alt S, Klaus-Bergmann A, Szymborska A, Zheng T, Perovic T, et al.
1290 Primary cilia sensitize endothelial cells to BMP and prevent excessive vascular
1291 regression. J Cell Biol [Internet]. 2018 May 7 [cited 2018 Sep 6];217(5):1651–65.
1292 Available from: http://www.ncbi.nlm.nih.gov/pubmed/29500191
1293 86. Simões FC, Riley PR. The ontogeny, activation and function of the epicardium during
1294 heart development and regeneration. Development [Internet]. 2018 Apr 1 [cited 2019
1295 Jul 30];145(7):dev155994. Available from:
1296 http://www.ncbi.nlm.nih.gov/pubmed/29592950
1297 87. Kikuchi K, Gupta V, Wang J, Holdway JE, Wills AA, Fang Y, et al. tcf21+ epicardial
1298 cells adopt non-myocardial fates during zebrafish heart development and regeneration.
1299 Development. 2011 Jul 15;138(14):2895–902.
1300 88. Jonassen JA, San Agustin J, Follit JA, Pazour GJ. Deletion of IFT20 in the mouse
1301 kidney causes misorientation of the mitotic spindle and cystic kidney disease. J Cell
1302 Biol [Internet]. 2008 Nov 3 [cited 2018 Sep 6];183(3):377–84. Available from:
1303 http://www.ncbi.nlm.nih.gov/pubmed/18981227
1304 89. Haycraft CJ, Zhang Q, Song B, Jackson WS, Detloff PJ, Serra R, et al. Intraflagellar
1305 transport is essential for endochondral bone formation. Development [Internet]. 2007
1306 Jan 15 [cited 2018 Sep 6];134(2):307–16. Available from:

1307 http://dev.biologists.org/cgi/doi/10.1242/dev.02732
1308 90. Holland AJ, Fachinetti D, Han JS, Cleveland DW. Inducible, reversible system for the
1309 rapid and complete degradation of proteins in mammalian cells. Proc Natl Acad Sci
1310 [Internet]. 2012 Dec 4 [cited 2018 Sep 14];109(49):E3350–7. Available from:
1311 http://www.ncbi.nlm.nih.gov/pubmed/23150568
1312 91. Cong L, Ran FA, Cox D, Lin S, Barretto R, Habib N, et al. Multiplex genome
1313 engineering using CRISPR/Cas systems. Science [Internet]. 2013 Feb 15 [cited 2018
1314 Sep 14];339(6121):819–23. Available from:
1315 http://www.ncbi.nlm.nih.gov/pubmed/23287718
1316 92. Pei Z, Bai Y, Schmitt AP. PIV5 M protein interaction with host protein angiomotin-
1317 like 1. Virology [Internet]. 2010 Feb 5 [cited 2018 Sep 6];397(1):155–66. Available
1318 from: http://linkinghub.elsevier.com/retrieve/pii/S0042682209006941
1319 93. Boin A, Couvelard A, Couderc C, Brito I, Filipescu D, Kalamarides M, et al. Proteomic
1320 screening identifies a YAP-driven signaling network linked to tumor cell proliferation
1321 in human schwannomas. Neuro Oncol [Internet]. 2014 Sep [cited 2018 Sep
1322 6];16(9):1196–209. Available from: https://academic.oup.com/neuro-oncology/article-
1323 lookup/doi/10.1093/neuonc/nou020
1324 94. He M, Subramanian R, Bangs F, Omelchenko T, Liem Jr KF, Kapoor TM, et al. The
1325 kinesin-4 protein Kif7 regulates mammalian Hedgehog signalling by organizing the
1326 cilium tip compartment. Nat Cell Biol [Internet]. 2014 Jul 22 [cited 2018 Sep
1327 6];16(7):663–72. Available from: http://www.ncbi.nlm.nih.gov/pubmed/24952464
1328